SUBSPACE METHODS FOR SOLVING ELECTROMAGNETIC INVERSE SCATTERING PROBLEMS[*]

XUDONG CHEN[†], YU ZHONG[†], AND KRISHNA AGARWAL[†]

Abstract. This paper presents a survey of the subspace methods and their applications to electromagnetic inverse scattering problems. Subspace methods can be applied to reconstruct both small scatterers and extended scatterers, with the advantages of fast speed, good stability, and higher resolution. For inverse scattering problems involving small scatterers, the multiple signal classification method is used to determine the locations of scatterers and then the least-squares method is used to calculate the scattering strengths of scatterers. For inverse scattering problems involving extended scatterers, the subspace-based optimization method is used to reconstruct the refractive index of scatterers.

Key words. Inverse scattering, optimization, subspace methods, electromagnetic wave scattering.

AMS subject classifications. 65K10, 65R32, 65Z05.

1. Introduction. Electromagnetic inverse scattering problems are considered in this paper. In recent years, subspace methods are widely used in solving electromagnetic inverse scattering problems. This paper presents a survey of the subspace methods for such applications. Generally speaking, in electromagnetic inverse scattering problems, scatterers can be categorized into two types: point-like scatterers and extended scatterers. A scatterer can be treated as point-like when its size is much smaller than one wavelength. When subspace methods are applied to reconstruct point-like scatterers, they are fast imaging methods since the nonlinear problem can be solved without iteratively evaluating the corresponding forward problem. In this survey, the multiple signal classification (MUSIC) method and the two-step least squares method are discussed, with the former being used to locate point-like scatterers and the latter being used to retrieve the scattering strengths of point-like scatterers. In reconstructing extended scatterers, the inverse scattering problems are usually cast into nonlinear optimization problems. The survey discusses the subspace-based optimization method (SOM). The method decomposes the solution space into two subspaces, so that the solution in one subspace is directly obtained from measured scattering data whereas the solution in the other subspace is obtained via iterative optimization. Since the optimization is carried out in a subspace instead of the whole space, the SOM is fast convergent. In addition, the SOM also has the advantage of being robust in presence of noise, high resolution, and the ability of reconstructing scatterers of complex patterns.

2. Reconstructing point-like scatterers.

2.1. Forward scattering problem. Consider M three-dimensional objects that are illuminated by time-harmonic electromagnetic waves radiated by an array of N antenna units (transceivers). The transceivers are located at $\overline{r}'_1, \overline{r}'_2, \ldots, \overline{r}'_N$, and each consists of 3 small dipole antennas oriented in the x, y and z directions with the transmitting current $I_x^{\mathrm{tran}}, I_y^{\mathrm{tran}}, I_z^{\mathrm{tran}}$, respectively. The M scatterers can be of any shape, but we consider only spherical objects here for ease of presenting. The size

---

of each scatterer is much smaller than the wavelength so that they can be treated as point-like scatterers. The centers of the scatterers are located at $\bar{r}_1, \bar{r}_2, \ldots, \bar{r}_M$. The shape and composing material of each small scatterer determine its polarization tensor $\overline{\overline{\xi}}$ [4] (that is also called the scattering strength tensor). Note that the time dependence factor $\exp(-i\omega t)$ for field quantities is assumed and is suppressed throughout the paper.

When multiple scattering between scatterers is taken into account, the total incident field $\bar{E}_t^{\mathrm{inc}}$ upon a scatterer includes both the incident field directly from antennas $\bar{E}_0^{\mathrm{inc}}$ and the scattered fields from other scatterers. The total incident fields are governed by the Foldy-Lax equation,

$$\bar{E}_t^{\mathrm{inc}} = \bar{E}_0^{\mathrm{inc}} + \overline{\overline{\Phi}} \cdot \overline{\overline{\Lambda}} \cdot \bar{E}_t^{\mathrm{inc}}, \tag{1}$$

where both $\overline{\overline{\Lambda}}$ and $\overline{\overline{\Phi}}$ are of size $3M \times 3M$. $\overline{\overline{\Lambda}} = \mathrm{diag}\left[\overline{\overline{\xi}}_1, \overline{\overline{\xi}}_2, \ldots, \overline{\overline{\xi}}_M\right]$ and $\overline{\overline{\Phi}}(j, j')$ is null for $j = j'$ and is $ik\overline{\overline{G}}(\bar{r}_j, \bar{r}_{j'})$ for $j \neq j'$, with k being the wavenumber and $\overline{\overline{G}}(\bar{r}, \bar{r}')$ being the dyadic Green's function in free space [28]. The incident field directly from transmitting antennas $\bar{E}_0^{\mathrm{inc}}$ is easily found to be

$$\bar{E}_0^{\mathrm{inc}} = \overline{\overline{R}}^{\mathrm{T}} \cdot \bar{I}^{\mathrm{tran}}, \tag{2}$$

where $\overline{\overline{R}}$ is of size $3N \times 3M$ with the submatrix in the ith row and jth column being $\overline{\overline{R}}(i, j) = ik\overline{\overline{G}}(\bar{r}_i', \bar{r}_j)$ and the superscript T denotes transpose. The scattered field is found to be

$$\bar{E}^{\mathrm{sca}} = \overline{\overline{R}} \cdot \overline{\overline{\Lambda}} \cdot \bar{E}_t^{\mathrm{inc}}, \tag{3}$$

The multi-static response (MSR) matrix that relates scattered fields to transmitting current is obtained by substituting (1) and (2) into (3):

$$\overline{\overline{K}} = \overline{\overline{R}} \cdot \overline{\overline{\Lambda}} \cdot (\overline{\overline{I}}_{3M} - \overline{\overline{\Phi}} \cdot \overline{\overline{\Lambda}})^{-1} \cdot \overline{\overline{R}}^{\mathrm{T}}, \tag{4}$$

where $\overline{\overline{I}}_{3M}$ is a $3M$-dimensional identity matrix. The MSR matrix is characteristic of the collection of scatterers for given sets of transceivers at the frequency of operation. The following notations will be used throughout the section. The $3N \times 3$ matrix $\overline{\overline{D}}_3(\bar{r})$ is defined as $\overline{\overline{D}}_3(\bar{r}) = ik\left[\overline{\overline{G}}^{\mathrm{T}}(\bar{r}_1', \bar{r}), \overline{\overline{G}}^{\mathrm{T}}(\bar{r}_2', \bar{r}), \ldots, \overline{\overline{G}}^{\mathrm{T}}(\bar{r}_N', \bar{r})\right]^{\mathrm{T}}$. The Green's function vector, $\bar{D}_x(\bar{r})$, $\bar{D}_y(\bar{r})$, and $\bar{D}_z(\bar{r})$ are defined through $\overline{\overline{D}}_3(\bar{r}) = [\bar{D}_x(\bar{r}), \bar{D}_y(\bar{r}), \bar{D}_z(\bar{r})]$. It is obvious that $\bar{D}_x(\bar{r})$, $\bar{D}_y(\bar{r})$, $\bar{D}_z(\bar{r})$, and $\overline{\overline{D}}_3(\bar{r})$ represent the Green's function observed at all the antennas due to a dipole source at the position $\bar{r}$, with the dipole oriented in the x, y, z, and all three directions, respectively.

2.2. Mathematical foundations. The key of the theoretical foundation lies in the injectivity of the so called current-to-field mapping operator, which is a map from the induced current (or secondary source) to the measured scattered field.

PROPOSITION. Define the operator $\Gamma: \mathbb{C}^{3M}$ to $\mathbb{C}^{3N}$ by

$$\lambda \mapsto \left\{ [(\Lambda\lambda)(\bar{r}_1')]^{\mathrm{T}}, [(\Lambda\lambda)(\bar{r}_2')]^{\mathrm{T}}, \ldots, [(\Lambda\lambda)(\bar{r}_N')]^{\mathrm{T}} \right\}^{\mathrm{T}}. \tag{5}$$

Then there exists $N_0 \in \mathbf{N}$ such that the operator Γ is one-to-one for $N \geq N_0$. Note that in (5) we have defined the operator Λ, which maps $\mathbb{C}^{3M}$ to the space $C(\mathbb{R}^3 \setminus \{\overline{r}_1, \overline{r}_2, \ldots, \overline{r}_M\})$ of continuous function on $\mathbb{R}^3 \setminus \{\overline{r}_1, \overline{r}_2, \ldots, \overline{r}_M\}$, by

$$(6) \qquad (\Lambda\lambda)(\overline{r}) := \sum_{j=1}^{M} \overline{\overline{G}}(\overline{r}, \overline{r}_j) \cdot \overline{a}_j$$

for $\overline{r} \in \mathbb{R}^3 \setminus \{\overline{r}_1, \overline{r}_2, \ldots, \overline{r}_M\}$, $\overline{a}_j \equiv [\lambda_{3j-2}, \lambda_{3j-1}, \lambda_{3j}]^{\mathrm{T}} \in \mathbb{C}^3$.

The proof of the above property directly follows [27] and is slightly different from [7]. It is sketched here for the reader's convenience.

Proof.

Step 1: We show that Λ is one-to-one. Let $\lambda \in \mathbb{C}^{3M}$, such that $(\Lambda\lambda)(\overline{r}) = 0$ for all $\overline{r} \in \mathbb{R}^3 \setminus \{\overline{r}_1, \overline{r}_2, \ldots, \overline{r}_M\}$. In case of $\overline{r}$ tending to one of the points $\overline{r}_j$, the fact that $\overline{\overline{G}}(\overline{r}, \overline{r}_j)$ approaches infinity yields that $\overline{a}_j = 0$ for every $j = 1, 2, \ldots, M$.

Step 2: Assume, without loss of generality, that the antenna array is on a spherical surface $S_{\rho_0} \equiv \{\overline{r} : (x^2 + y^2 + z^2)^{1/2} = \rho_0\}$, where ρ_0 is large enough to enclose all M sources. Consider $\{\overline{r}'\}_n \subset S_{\rho_0}$ be a countable set of positions with the property that any analytic function which vanishes in $\overline{r}'_n$ for all $n \in \mathbf{N}$ vanishes identically on the spherical surface S_{ρ_0}.

We prove the proposition by contradiction. If there existed no such N_0, then there would exist sequences $\{N_l\}$ in $\mathbf{N}$ and $\{\lambda^{(l)}\}$ in $\mathbb{C}^{3M}$ with $\sum_{j=1}^{3M} |\lambda_j^{(l)}| = 1$ and $(\Lambda\lambda^{(l)})(\overline{r}'_p) = 0$ for all $p = 1, 2, \ldots, N_l$. The sequence $\{\lambda^{(l)}\}$ has accumulation points. We assume that $\lambda^{(l)} \to \lambda$ as $l \to \infty$, with $\sum_{j=1}^{3M} |\lambda_j| = 1$. For any $n \in \mathbf{N}$ and l with $N_l \geq n$, we estimate by the triangle inequality

$$|(\Lambda\lambda)(\overline{r}'_n)| \leq \left| \sum_{j=1}^{M} \overline{\overline{G}}(\overline{r}'_n, \overline{r}_j) \cdot \overline{a}_j - \sum_{j=1}^{M} \overline{\overline{G}}(\overline{r}'_n, \overline{r}_j) \cdot \overline{a}_j^{(l)} \right| + \left| \sum_{j=1}^{M} \overline{\overline{G}}(\overline{r}'_n, \overline{r}_j) \cdot \overline{a}_j^{(l)} \right|$$

$$(7) \qquad = \sum_{j=1}^{M} \left| \overline{\overline{G}}(\overline{r}'_n, \overline{r}_j) \cdot (\overline{a}_j - \overline{a}_j^{(l)}) \right| \leq C \sum_{j=1}^{M} \left| \overline{a}_j - \overline{a}_j^{(l)} \right|$$

for some finite constant C independent of l, and this converges to zero as l tends to infinity. Therefore, $(\Lambda\lambda)(\overline{r}'_n) = 0$ for every $n \in \mathbf{N}$. Since $\Lambda\lambda$ is analytic on S_{ρ_0}, we conclude, by our assumption, that $\Lambda\lambda$ vanishes on all of points on the spherical surface S_{ρ_0}. By Huygens's principle [28], we conclude that the far field electric field vanishes identically. Then by Rellich's lemma [19], $(\Lambda\lambda)(\overline{r}) = 0$ for all $\overline{r} \in \mathbb{R}^3 \setminus \{\overline{r}_1, \overline{r}_2, \ldots, \overline{r}_M\}$, which yields $\lambda = 0$ by the first part of the proof. This contradicts the fact that $\sum_{j=1}^{3M} |\lambda_j^{(l)}| = 1$. The proof is complete. $\square$

As corollaries, the injectivity of the current-to-intensity operator Γ theoretically justifies the position-locating work via MUSIC method and the polarization-tensor-retrieval work via two-step least squares method. It is stressed that this injectivity is independent of the number of scatterers, i.e., it is valid for any positive integer M.

2.2.1. Locating positions. Positions of point-like scatterers can be found by MUSIC method, and its basic principle is summarized as follows. Suppose $\overline{a} \in \mathbb{C}^3 \setminus \{0\}$ and the size, $3N$, of the MSR matrix $\overline{\overline{K}}$ is sufficiently large, then for any position $\overline{r}$,

$$(8) \qquad \overline{\overline{D}}_3(\overline{r}) \cdot \overline{a} \in \mathcal{R}(\overline{\overline{K}}) \quad \text{iff} \quad \overline{r} \in \{\overline{r}_1, \overline{r}_2, \ldots, \overline{r}_M\},$$

where $\mathcal{R}(\cdot)$ denotes the range. This statement is in fact a corollary of the aforementioned proposition, considering the fact that the range of $\overline{\overline{K}}$ is the span of the columns of $\overline{\overline{D}}_3(\overline{r}_j)$, $j = 1, 2, \ldots, M$, i.e., $\bar{D}_x(\overline{r}_j), \bar{D}_y(\overline{r}_j), \bar{D}_z(\overline{r}_j)$.

Proof of sufficient condition. If, for example, $\overline{r} = \overline{r}_1$, the obvious choice of zeroing coefficients of all $\overline{\overline{D}}_3(\overline{r}_j)$ except $\overline{\overline{D}}_3(\overline{r}_1)$ satisfies the condition.

Proof of necessary condition. Assume, to the contrary, that there is an $\overline{r}_0$ that is different from $\overline{r}_1, \overline{r}_2, \ldots, \overline{r}_M$ and $\overline{\overline{D}}_3(\overline{r}_0) \cdot \overline{a}$ for some $\overline{a}$ is in the range of $\overline{\overline{K}}$. Thus, the new set of Green's function vectors $\overline{\overline{D}}_3(\overline{r}_j)$, $j = 0, 1, 2, \ldots, M$, corresponding to the group of $M + 1$ points $\{\overline{r}_0, \overline{r}_1, \overline{r}_2, \ldots, \overline{r}_M\}$ is linear dependent, which however contradicts the injectivity of Γ.

2.2.2. Retrieving polarization tensors. As to retrieving the polarization tensor, the injectivity of Γ simply implies that the coefficient $\lambda \in \mathbb{C}^{3M}$ can be uniquely determined from (5) once the scattered field ($\in \mathbb{C}^{3N}$) is measured, which is the first and the most important step in the two-step retrieval method presented in [43, 2].

2.3. MUSIC algorithm: Locating positions. The multiple signal classification (MUSIC) algorithm [37, 20, 5, 6] has been of great interest in the inverse scattering community since it was proposed to locate point-like scatterers in 2000 [20]. Positions of the small objects are retrieved from the multistatic response (MSR) matrix generated by an array of transceivers [21, 22, 38, 27, 7]. MUSIC imaging method was first applied to acoustic imaging, where scalar field is involved. The test function used to generate the MUSIC pseudo-spectrum is the Green's function of the background medium associated with a monopole source [18, 22, 27]. Recently, MUSIC algorithm was generalized to electromagnetic imaging of small three-dimensional targets [7, 26, 43].

2.3.1. Standard MUSIC algorithm. The MSR matrix $\overline{\overline{K}}$ maps $\mathbb{C}^{3N}$, the vector space of complex $3N$-tuples, to its range $S_r \subseteq \mathbb{C}^{3N}$. From the singular value decomposition (SVD) analysis [24], the MSR matrix could be represented as $\overline{\overline{K}} \cdot \bar{v}_p = \sigma_p \bar{u}_p$ and $\overline{\overline{K}}^* \cdot \bar{u}_p = \sigma_p \bar{v}_p$, $p = 1, 2, \ldots, 3N$, where the superscript $*$ denotes the Hermitian. The vector space $\mathbb{C}^{3N}$ can be decomposed into the direct sum of the range (subspace) $S_r = \text{span}\{\bar{u}_p, \sigma_p > 0\}$ and the orthogonal complement subspace $S_n = \text{span}\{\bar{u}_p, \sigma_p = 0\}$ that is referred to as noise subspace. Consider non-degenerate scatterers in the absence of noise, three independent electric current dipole components are induced in each scatterer, and the scattered field $\bar{E}^{\text{sca}}$ is in the space S_0 spanned by the background Green's function vectors associated with the x, y, and z components of electric dipoles evaluated at the position of each scatterer, i.e., $\bar{E}^{\text{sca}} \in S_0 = \text{span}\left\{\bar{D}_x(\overline{r}_j), \bar{D}_y(\overline{r}_j), \bar{D}_z(\overline{r}_j); j = 1, 2, \ldots, M\right\}$. In this case, it is easy to conclude that two subspaces S_r and S_0 are identical [21, 22, 43]. Due to the orthogonality between the range S_r and the noise space S_n, we have $\left|\bar{u}_p^* \bar{D}_l(\overline{r}_m)\right| = 0$ and for $\sigma_p = 0$, $m = 1, 2, \ldots, M$ and $l = x, y, z$. The standard MUSIC algorithm [7, 26, 43] defines the following pseudo-spectrum

$$(9) \qquad \Phi(\overline{r}) = \frac{1}{\sum_{\sigma_p=0} \left|\bar{u}_p^* \bar{f}(\overline{r})\right|^2},$$

where test function $\bar{f}(\overline{r})$ can be any linear combination of $\bar{D}_x(\overline{r})$, $\bar{D}_y(\overline{r})$, and $\bar{D}_z(\overline{r})$. The pseudo-spectrum becomes infinite at the position of every scatterer.

2.3.2. MUSIC algorithm with the optimal test dipole direction. In standard MUSIC, the test dipole can be oriented in any direction in noise free case for non-degenerate scatterers, defined as those inside which three independent components of an electric dipole are induced. Inside degenerate scatterers, only one or two independent components of an electric dipole are induced due to special shapes or composing materials of the scatterers. For example, a needle-like or disk-like small object may present only one or two dominant components of induced electric dipoles. In degenerate cases, the standard MUSIC does not work since an arbitrarily chosen direction of test dipole is not necessarily located in the space spanned by actually induced independent dipole components [10]. In addition, even for non-degenerate scatterers, when scattered fields are noise contaminated, the performance of the MUSIC algorithm is found to noticeably depend on the orientation of the test dipole. Here, we introduce an algorithm to find the optimal test dipole direction which not only obtains a good imaging resolution but also is able to deal with degenerate scatterers.

To find the optimal test dipole direction is equivalent to determine $\overline{a} \in \mathbb{C}^3$ subject to $||\overline{a}|| = 1$, so that the solution $\bar{x}$ to the equation

$$\overline{\overline{K}} \cdot \bar{x} = \overline{\overline{D}}_3(\overline{r}) \cdot \overline{a} \tag{10}$$

is most robust in the presence of noise. The SVD of $\overline{\overline{K}}$ is given by

$$\overline{\overline{K}} = \sum_{i=1}^{3N} \bar{u}_i \sigma_i \bar{v}_i^*. \tag{11}$$

Assume singular values are in non-increasing order, $\sigma_1 \geq \sigma_2 \geq \ldots, \geq \sigma_{3N} \geq 0$. The least squares solution of $\bar{x}$ is given by

$$\bar{x} = \sum_{i=1}^{3N} \frac{\bar{u}_i^* \cdot \overline{\overline{D}}_3(\overline{r}) \cdot \overline{a}}{\sigma_i} \bar{v}_i. \tag{12}$$

Note that the value of $\frac{1}{\sigma_i}$ is large for a small σ_i. To obtain a stable solution $\bar{x}$, we should find $\overline{a}$ so that $\bar{u}_i^* \cdot \overline{\overline{D}}_3(\overline{r}) \cdot \overline{a}$ is non-zero for only the first few items. It is worth mentioning that even in case of truncated singular value decomposition, i.e., regularization method is used, it is desirable to have a fast decaying series of $\bar{u}_i^* \cdot \overline{\overline{D}}_3(\overline{r}) \cdot \overline{a}$. Due to the orthogonality of $\bar{u}_i$, we need to find $\overline{a}$ so that $\overline{\overline{D}}_3(\overline{r}) \cdot \overline{a}$ is a linear combination of the first few (say L) $\bar{u}_i$.

$$\sum_{i=1}^{L} \lambda_i \bar{u}_i = \overline{\overline{D}}_3(\overline{r}) \cdot \overline{a}. \tag{13}$$

The new MUSIC algorithm is based on the analysis of the induced electric current dipoles in the eigenstate, which is referred to as the eigen-dipole hereafter. We use $\overline{J}_j^{(i)}$ to denote the current in the jth scatterer in the ith eigen-state. We have

$$\bar{u}_i = \sum_{j=1}^{M} \overline{\overline{D}}_3(\overline{r}_j) \cdot \overline{J}_j^{(i)}, \quad i = 1, 2, \ldots, L. \tag{14}$$

The substitution of (14) into (13) yields

$$(15) \qquad \sum_{j=1}^{M} \overline{\overline{D}}_3(\overline{r}_j) \cdot \sum_{i=1}^{L} \lambda_i \overline{J}_j^{(i)} = \overline{\overline{D}}_3(\overline{r}) \cdot \overline{a}.$$

There are two cases to be considered: (a) when the test position $\overline{r}$ is not at any of the scatterers, $\overline{r}_j$, and (b) $\overline{r}$ is at one of the scatterers.

It is important to stress that the map from induced currents to scattered electric fields is one-to-one [27, 7]. The proof is given in Section 2.2. When the test position $\overline{r}$ is not at any of the scatterers, (15) holds only if $\overline{a} = 0$ and $\lambda_i = 0$. Therefore, for any dipole direction $\overline{a}$, which satisfies $||\overline{a}|| = 1$, $\bar{u}_i^* \cdot \overline{\overline{D}}_3(\overline{r}) \cdot \overline{a}$ is not equal to zero for all $3N$ left singular vectors $\bar{u}_i$. In this case, the solution $\bar{x}$ is the linear combination of all $3N$ right singular vectors $\bar{v}_i$ as shown in (12). It is obvious that the resultant least squares solution is not stable due to the presence of small σ_i.

When $\overline{r}$ is at one of the scatterers, for example, $\overline{r} = \overline{r}_1$, (15) requires

$$(16) \qquad \sum_{i=1}^{L} \overline{J}_1^{(i)} \lambda_i = \overline{a},$$

$$(17) \qquad \sum_{i=1}^{L} \overline{J}_j^{(i)} \lambda_i = 0, \quad j = 2, 3, \ldots, M.$$

Eq. (17) amounts to determining the minimum value of L so that $\overline{J}^{(1)}$, $\overline{J}^{(2)}$, ..., $\overline{J}^{(L)}$ are linearly dependent, where $\overline{J}^{(i)}$ is a column vector of length $3(M-1)$ consisting of $\overline{J}_j^{(i)}$, $j = 2, 3, \ldots, M$. Therefore, when the test point $\overline{r}$ is at one of the scatterers, the value of minimum L is equal to one plus the total number of independent dipoles induced in other scatterers. For example, for M isotropic spheres, the value of L equals to $3M - 2$. It is stressed that the algorithm also applies to degenerate cases. When the nontrivial λ_i, $i = 1, 2, \ldots, L$ obtained from (17) are plugged into (16), the resulting $\overline{a}$ is generally a complex value. When we force the vector $\overline{a}$ to be real, more eigen-states are needed to solve (16) and (17). Thus from (12), we know that the solution is not as robust as the one obtained from the previous complex $\overline{a}$.

In practice, the value of L can be easily obtained after the total number of dominant singular values is found from the spectrum. From the previous analysis, it is easy to conclude that the value of L is equal to the total number of dominant singular values, or it minus one or two, depending on the case of degeneracy of scatterers. The test dipole direction is determined by finding $\overline{a} \in \mathbb{C}^3$ subject to $||\overline{a}|| = 1$, so that $\overline{\overline{D}}_3(\overline{r}) \cdot \overline{a}$ is close to the space spanned by the first L dominant singular vectors $\bar{u}_i$, i.e., we aim at a minimum projection angle between the vector $\overline{\overline{D}}_3(\overline{r}) \cdot \overline{a}$ and the space spanned by the singular vectors $\bar{u}_i$, $i = 1, 2, \ldots, L$:

$$(18) \qquad \overline{a}_{\mathrm{max}} = \arg\max_{\overline{a}} \frac{\sum_{i=1}^{L} |\bar{u}_i^* \cdot \overline{\overline{D}}_3(\overline{r}) \cdot \overline{a}|^2}{|\overline{\overline{D}}_3(\overline{r}) \cdot \overline{a}|^2}.$$

From the general eigenvalue decomposition, we obtained the solution $\overline{a}$ that is given by the eigenvector corresponding to the maximum eigenvalue of the matrix $\left(\overline{\overline{D}}_3(\overline{r})^* \cdot \overline{\overline{D}}_3(\overline{r}) \right)^{-1} \left(\left[\overline{\overline{U}} \cdot \overline{\overline{D}}_3(\overline{r}) \right]^* \left[\overline{\overline{U}} \cdot \overline{\overline{D}}_3(\overline{r}) \right] \right)$, where $\overline{\overline{U}} = [\bar{u}_1, \bar{u}_2, \ldots, \bar{u}_L]^*$. It

should be noted that when the test vector $\bar{a}$ is restricted to be real, the solution to (18) is given by the eigenvector corresponding to the maximum eigenvalue of the matrix $\left[\mathbb{R} \left(\overline{\overline{D}}_3(\bar{r})^* \overline{\overline{D}}_3(\bar{r}) \right) \right]^{-1} \cdot \mathbb{R} \left(\left[\overline{\overline{U}} \cdot \overline{\overline{D}}_3(\bar{r}) \right]^* \left[\overline{\overline{U}} \cdot \overline{\overline{D}}_3(\bar{r}) \right] \right)$, where $\mathbb{R}(\cdot)$ denotes the real part operator. Then, the pseudo-spectrum can be defined as

$$
(19) \qquad \Phi(\bar{r}) = \frac{1}{1 - \frac{\sum_{i=1}^{L} |\bar{u}_i^* \cdot \overline{\overline{D}}_3(\bar{r}) \cdot \bar{a}_{\max}|^2}{|\overline{\overline{D}}_3(\bar{r}) \cdot \bar{a}_{\max}|^2}},
$$

which peaks at the position of every scatterer.

2.4. Two-step least squares: Retrieving polarization tensors. Once the positions of point-like scatterers are located, we are able to retrieve the polarization tensors of scatterers. It is stressed that this is a nonlinear problem when multiple scattering effect is considered. A common approach to such a nonlinear problem is to cast it into an optimization problem and the corresponding forward problem is iteratively evaluated during the optimization process. However, this approach is time consuming and the optimization results depend, to a great extent, on the initial guess.

However, such a nonlinear problem can be solved noniteratively. As shown in Section 2.2.2, the injectivity of Γ simply implies that the coefficient λ can be uniquely determined from (5). Following this guideline, the polarization tensors of scatterers can be retrieved noniteratively, which is outlined as follows. From (3), the induced current (secondary source) $\overline{\overline{\Lambda}} \cdot \bar{E}_t^{\text{inc}}$ can be uniquely determined from the scattered field $\bar{E}^{\text{sca}}$.

$$
(20) \qquad \overline{\overline{\Lambda}} \cdot \bar{E}_t^{\text{inc}} = \overline{\overline{R}}^{\dagger} \cdot \bar{E}^{\text{sca}},
$$

where $\dagger$ denotes the least-square based inverse. In the second step, we multiply both sides of (1) by $\overline{\overline{\Lambda}}$,

$$
(21) \qquad \overline{\overline{\Lambda}} \cdot \bar{E}_t^{\text{inc}} = \overline{\overline{\Lambda}} \cdot \left(\bar{E}_0^{\text{inc}} + \overline{\overline{\Phi}} \cdot \overline{\overline{\Lambda}} \cdot \bar{E}_t^{\text{inc}} \right).
$$

The polarization tensor matrix $\overline{\overline{\Lambda}}$ is obtained, with the aid of (20),

$$
(22) \qquad \overline{\overline{\Lambda}} = \left(\overline{\overline{\Lambda}} \cdot \bar{E}_t^{\text{inc}} \right) \cdot \left(\bar{E}_0^{\text{inc}} + \overline{\overline{\Phi}} \cdot \overline{\overline{\Lambda}} \cdot \bar{E}_t^{\text{inc}} \right)^{\dagger}.
$$

Thus, the two-step least squares method solves the nonlinear inverse problem noniteratively.

The retrieval algorithms presented in [43, 9, 2, 10] all follow the aforementioned guideline. It is worth mentioning that the first non-iterative algorithm was proposed in [30], and it was different from the two-step least squares method. The numerical simulation conducted in [9] showed that the two-step least squares method performed better than the first non-iterative algorithm.

2.5. Reconstructing point-like scatterers: Phaseless data. When only the intensity of scattered field is measured, the inverse scattering problem of determining the locations and scattering strengths is more difficult to solve. The Green's function vectors $\bar{D}_x(\bar{r}_j), \bar{D}_y(\bar{r}_j), \bar{D}_z(\bar{r}_j),\ j = 1, 2, \ldots, M$, do not form the linear basis of the measured intensity data any more. Nevertheless, [31] and [11] constructed the linear basis of the phaseless data: $\bar{D}_x(\bar{r}_i) \circ \bar{D}_y(\bar{r}_j)^*,\ \bar{D}_y(\bar{r}_i) \circ \bar{D}_z(\bar{r}_j)^*,\ \bar{D}_z(\bar{r}_i) \circ \bar{D}_x(\bar{r}_j)^*,\ i, j =$

$1, 2, \ldots, M$, where $\circ$ denotes Hadamard product (or Schur product) that is an element-wise product. The superscript * denotes complex conjugate. In MUSIC algorithm that is presented in [31], the aforementioned basis span a subspace that coincides with the range (subspace) of the resultant MSR matrix.

After obtaining the locations of point-like scatterers, a three-step noniterative retrieval algorithm is applied to solve the nonlinear problem of determining the polarization tensors of scatterers, with multiple scattering taken into account [11]. The first and third steps are similar to the two-step retrieval method for full scattering data, whereas the second step is new and is to find the constant phase factor.

To summarize, for phaseless inverse scattering problems for point-like scatterers, even if multiple scattering effect is taken into account, the locations and scattering strengths of point-like scatterers can be obtained without iteratively evaluating the corresponding forward problem.

3. Reconstructing extended scatterers. When the scatterer's size is comparable to wavelength, the inverse scattering problem is significantly different from the one for point-like scatterers. For extended scatterers, it is well known that the source-to-field operator (see (5)) is compact. In another word, it is impossible to uniquely determine the value of λ from (5) when M approaches infinity. However, a portion of λ can be uniquely obtained from a subspace of the domain of the operator Γ. This subspace is spanned by singular vectors of Γ associated with few leading singular values. Following this guideline, we proposed a subspace-based optimization method (SOM) for solving the two-dimensional (2D) electromagnetic inverse scattering problems [12, 13] and the 3D problem [44], i.e., reconstructing the dielectric profile of scatterers from scattered fields. By using the spectral property of the current-to-field mapping operator, the SOM first determines part of the induced current, the deterministic part, and then obtains the rest part, the ambiguous part of the induced current, via optimization. Since the optimization is carried out in a subspace of the current space, the SOM actually simplifies the nonlinear optimization problem.

Based on the SOM, we further analyze the spectral property of the mapping from the induced current to the scattered fields inside the domain of interest. We find that, the current subspace could be shrunk to a much smaller one so that the optimization of the induced current is regularized in a proper way which increases the stability of the inversion and the robustness against the noise compared to the original SOM. Since a secondfold subspace constraint is used, this method is referred to as the twofold SOM (TSOM) [45].

In this section, we first introduce the SOM in both 2D transverse magnetic (TM) and 3D cases. Then, the TSOM is discussed. Here, the forward problem is solved in the framework of the method of moments (MOM), which however is not a necessity and can be replaced by other numerical models, such as the coupled dipole method (CDM).

In both 2D and 3D cases, the domains of interest are chosen to be rectangular and cuboid in order to implement the conjugate gradient fast Fourier transform (CG-FFT) scheme. For the convenience of reading, we denote the one-dimensional tensor as $\overline{a}$, two-dimensional tensor as $\overline{\overline{a}}$, three-dimensional tensor as $\hat{a}$, and four-dimensional tensor as $\hat{\hat{a}}$. Unless otherwise specified, the subscript of the tensors denotes the index of the element, such as $\overline{\overline{a}}_{m,n}$ denotes the element in $\overline{\overline{a}}$ with index $\{m, n\}$. We use bold symbols to denote vector quantities, such as the positions $\boldsymbol{r}$ and the electric fields $\boldsymbol{E}$ in 3D case.

3.1. 2D TM SOM. Assume that there are N_i incident waves from different angles onto the rectangular domain of interest $\mathcal{D}$ ($\mathcal{D} \subset \mathcal{R}^2$, the background 2D homogeneous medium with permittivity ϵ_0, permeability μ_0, and wave number k_0), where nonmagnetic scatterers are located, and these incident waves are expressed as $E_l^{\mathrm{inc}}(\boldsymbol{r})$, $l = 1, 2, \ldots, N_\mathrm{i}$, $\boldsymbol{r} \in \mathcal{D}$. For each incidence, the scattered fields are detected by N_r antennas located at $\boldsymbol{r}'_j$, $j = 1, 2, \ldots, N_\mathrm{r}$. With all these information, including every incident field inside the domain of interest and the corresponding scattered fields at the positions of all detectors, we aim at retrieving the dielectric profile $\epsilon(\boldsymbol{r})$, $\boldsymbol{r} \in \mathcal{D}$. The governing equation inside the domain of interest is the Lippmann-Schwinger equation. From the Lippmann-Schwinger equation or the electric field integral equation (EFIE) in TM scenario, for the lth incidence ($l = 1, 2, \ldots, N_\mathrm{i}$), the induced current satisfies (23),

$$(23) \qquad [\epsilon_\mathrm{r}(\boldsymbol{r}) - 1]\, E_l^{\mathrm{inc}}(\boldsymbol{r}) = \frac{I_l(\boldsymbol{r})}{-i\omega\epsilon_0} - [\epsilon_\mathrm{r}(\boldsymbol{r}) - 1]\, i\omega\mu_0 \int_{\mathcal{D}} g(\boldsymbol{r}, \boldsymbol{r}') I_l(\boldsymbol{r}')d\boldsymbol{r}',$$

where $i = \sqrt{-1}$, $g(\boldsymbol{r}, \boldsymbol{r}') = \frac{i}{4} H_0^{(1)}(k_0\, |\boldsymbol{r} - \boldsymbol{r}'|)$ is the 2D Green's function of the background medium, $\epsilon_\mathrm{r}(\boldsymbol{r}) = \epsilon(\boldsymbol{r})/\epsilon_0$ is the relative permittivity at $\boldsymbol{r}$, and

$$(24) \qquad\qquad I_l(\boldsymbol{r}) = -i\omega\epsilon_0 \left[\epsilon_\mathrm{r}(\boldsymbol{r}) - 1\right] E_l(\boldsymbol{r})$$

is the induced current while $E_l(\boldsymbol{r})$ is the electric field at $\boldsymbol{r}$ [35]. For the convenience of computing, the domain of interest $\mathcal{D}$ is discretized into many small subdomains whose dimensions are much smaller than the wavelength and whose centers are located at, say, $\boldsymbol{r}_{m,n}$, $m = 1, 2, \ldots, M_1$ and $n = 1, 2, \ldots, M_2$, where M_1 and M_2 are the total number of subdomains along x and y axes, respectively (so that, the total number of subdomains is $M = M_1 \times M_2$). Thus the continuous integral operator in Lippmann-Schwinger equation becomes a summation of contributions from every subdomain. By approximating every subdomain as a small circle with an equivalent radius $a_{m,n} = \sqrt{S_{m,n}/\pi}$, where $S_{m,n}$ is the area of the subdomain with index (m, n), $m = 1, 2, \ldots, M_1$, $n = 1, 2, \ldots, M_2$, and its center at $\boldsymbol{r}_{m,n}$, we discretize (23) as

$$(25) \qquad\qquad \overline{\overline{\chi}}_{m,n} \overline{\overline{E}}_{l;m,n}^{\mathrm{inc}} = \frac{\overline{\overline{I}}_{l;m,n}}{-i\omega\epsilon_0} - \overline{\overline{\chi}}_{m,n} \overline{\overline{A}}_{m,n}(\overline{\overline{I}}_l),$$

where $\overline{\overline{\chi}}_{m,n} = \overline{\overline{\epsilon}}_{\mathrm{r};m,n} - 1$ is the contrast at $\boldsymbol{r}_{m,n}$, $\epsilon_{\mathrm{r};m,n}$ is the relative permittivity at $\boldsymbol{r}_{m,n}$, $\overline{\overline{E}}_{l;m,n}^{\mathrm{inc}}$ is the incident electric field at $\boldsymbol{r}_{m,n}$, $\overline{\overline{I}}_{l;m,n}$ is the induced current at $\boldsymbol{r}_{m,n}$, and $\overline{\overline{A}}$ is an operator defined by

$$(26) \qquad\qquad \overline{\overline{A}}_{m,n}(\overline{\overline{I}}_l) = \sum_{m'=1}^{M_1} \sum_{n'=1}^{M_2} G_\mathrm{D}(\boldsymbol{r}_{m,n}, \boldsymbol{r}_{m',n'}) \overline{\overline{I}}_{l;m',n'},$$

with $G_\mathrm{D}(\boldsymbol{r}_{m,n}, \boldsymbol{r}_{m',n'})$ being the integral of the Green's function [35]. All the two dimensional tensors in (25) are with size $M_1 \times M_2$. Similarly, the integral operator relating the induced current and the scattered fields could also be expressed as the summation of the contribution from all the subdomains,

$$(27) \qquad\qquad \overline{E}_l^{\mathrm{sca}} = \overline{\overline{G}}_\mathrm{S} \cdot \overline{I}_l,$$

where $\overline{E}_l^{\text{sca}} = \left[E_l^{\text{sca}}(\boldsymbol{r}_1'), E_l^{\text{sca}}(\boldsymbol{r}_2'), \ldots, E_l^{\text{sca}}(\boldsymbol{r}_{N_{\text{r}}}')\right]^{\text{T}}$, $\overline{I}_l = \operatorname{vec}\left\{\overline{\overline{I}}_l\right\}$ is an M dimensional vector, and $\overline{\overline{G}}_{\text{S}}$ is a $N_{\text{r}} \times M$ matrix with its elements $\overline{\overline{G}}_{\text{S};j,q} = -\frac{\eta_0 \pi a_{m,n}}{2} J_1(k_0 a_{m,n}) H_0^{(1)}(k_0 \left|\boldsymbol{r}_j' - \boldsymbol{r}_{m,n}\right|)$ for $j = 1, 2, \ldots, N_{\text{r}}$, $q = m + (n-1) \times M_1$, $m = 1, 2, \ldots, M_1$ and $n = 1, 2, \ldots, M_2$. Here, $\operatorname{vec}\{\cdot\}$ denotes the operation of vectorizing a tensor, i.e., in this case, $\overline{I}_{l;q} = \overline{\overline{I}}_{l;m,n}$ with $q = m + (n-1) \times M_1$.

Since the inverse scattering problem for extended scatterers is usually underdetermined, i.e. N_{r} and N_{i} are both much smaller than M, and due to the fact that $\overline{\overline{G}}_S$ contains zero and very small singular values, it is impossible to directly determine $\overline{I}_l$ from (27). Thus, it is convenient to split the induced current into two parts: a deterministic part $\overline{I}_l^{\text{d}}$ and an ambiguous part $\overline{I}_l^{\text{a}}$, the former of which could be obtained from (27) and the later by the optimization method [12]. The singular value decomposition of $\overline{\overline{G}}_{\text{S}}$ tells $\overline{\overline{G}}_{\text{S}} \cdot \overline{v}_j^{\text{S}} = \sigma_j^{\text{S}} \overline{u}_j^{\text{S}}$, $j = 1, 2, \ldots, M$, with the bases $\overline{v}_j^{\text{S}}$ spanning the current space while $\overline{u}_j^{\text{S}}$ the scattered field space. Here the superscript S denotes the mapping $\overline{\overline{G}}_{\text{S}}$. Assuming that the singular values are a non-increasing sequence, i.e. $\sigma_m^{\text{S}} \geq \sigma_n^{\text{S}}$ if $m < n$, the first L (since $L \leq N_{\text{r}}$) current bases, $\overline{v}_j^{\text{S}}$, $j = 1, 2, \ldots, L$, construct a current subspace that is the most influential to the scattered fields. Thus, from (27), we have

$$(28) \qquad \overline{I}_l^{\text{d}} = \sum_{j=1}^{L} \frac{\overline{u}_j^{\text{S}*} \cdot \overline{E}_l^{\text{sca}}}{\sigma_j^{\text{S}}} \overline{v}_j^{\text{S}} = \overline{\overline{V}}_{\text{S}}^{+} \cdot \overline{\alpha}_l^{+},$$

where $\overline{\overline{V}}_{\text{S}}^{+} = \left[\overline{v}_1^{\text{S}}, \overline{v}_2^{\text{S}}, \ldots, \overline{v}_L^{\text{S}}\right]$, $\overline{\alpha}_l^{+} = \left[\alpha_{l;1}^{+}, \alpha_{l;2}^{+}, \ldots, \alpha_{l;L}^{+}\right]^{\text{T}}$ with $\alpha_{l;j}^{+} = (\overline{u}_j^{\text{S}*} \cdot \overline{E}_l^{\text{sca}})/\sigma_j^{\text{S}}$, $j = 1, 2, \ldots, L$, and the superscript $*$ denotes the Hermitian operation while superscript $+$ refers to the dominant current subspace, the subspace corresponding to the dominant singular values. From (28), we clearly see that in order to reduce the impact of noise contained in the contaminated measured $\overline{E}_l^{\text{sca}}$, it is necessary to choose an appropriate value of L so that the σ_L^{S} is above the level of noise. On the other hand, in [12], the ambiguous part of the current is expressed by the rest $M - L$ bases,

$$(29) \qquad \overline{I}_l^{\text{a}} = \sum_{j=1}^{M-L} \overline{v}_{j+L}^{\text{S}} \alpha_{l;j}^{-} = \overline{\overline{V}}_{\text{S}}^{-} \cdot \overline{\alpha}_l^{-},$$

where $\overline{\overline{V}}_{\text{S}}^{-} = \left[\overline{v}_{L+1}^{\text{S}}, \overline{v}_{L+2}^{\text{S}}, \ldots, \overline{v}_M^{\text{S}}\right]$ and $\overline{\alpha}_l^{-} = \left[\alpha_{l;1}^{-}, \alpha_{l;2}^{-}, \ldots, \alpha_{l;M-L}^{-}\right]^{\text{T}}$, with the latter being the unknown coefficients. Here the superscript $-$ refers to the subordinate current subspace, the subspace corresponding to those subordinate singular values. In [44], by using the identity $\overline{\overline{V}}_{\text{S}}^{-} \cdot \overline{\overline{V}}_{\text{S}}^{-*} = \overline{\overline{I}}_M - \overline{\overline{V}}_{\text{S}}^{+} \cdot \overline{\overline{V}}_{\text{S}}^{+*}$, where $\overline{\overline{I}}_M$ is the M dimensional identity matrix, the authors propose a new current construction method as follows

$$(30) \qquad \begin{aligned} \overline{I}_l^{\text{a}}(\overline{\beta}_l) &= \overline{\overline{V}}_{\text{S}}^{-} \cdot \overline{\alpha}_l^{-} \\ &= \overline{\overline{V}}_{\text{S}}^{-} \cdot \overline{\overline{V}}_{\text{S}}^{-*} \cdot \overline{\beta}_l \\ &= \left(\overline{\overline{I}}_M - \overline{\overline{V}}_{\text{S}}^{+} \cdot \overline{\overline{V}}_{\text{S}}^{+*}\right) \cdot \overline{\beta}_l, \\ &= \overline{\beta}_l - \overline{\overline{V}}_{\text{S}}^{+} \cdot \left(\overline{\overline{V}}_{\text{S}}^{+*} \cdot \overline{\beta}_l\right) \end{aligned}$$

in which we let $\overline{\alpha}_l^{-} = \overline{\overline{V}}_{\text{S}}^{-*} \cdot \overline{\beta}_l$ (This is reasonable since the rank of $\overline{\overline{V}}_{\text{S}}^{-*}$ is $M - L$). In this new current expression, $\overline{\beta}_l$ becomes the unknowns instead of $\overline{\alpha}_l^{-}$. Though

the number of the unknowns increases ($\overline{\beta}_l$ is an M dimension vector while $\overline{\alpha}_l^-$ is an $M - L$ dimension vector), the computational complexity of the current construction decreases dramatically. Besides, since only the first L singular vectors are needed, a thin SVD operation (generating only those singular vectors with non-null singular values) is enough. Having expressed the induced current in the aforementioned way, it is convenient to define the objective function. Firstly, it is natural to define the mismatch of the scattered fields by

$$(31) \qquad \Delta_l^{\text{fie}}(\overline{\beta}_l) = \left\| \overline{\overline{G}}_{\text{S}} \cdot \overline{I}_l^{\text{a}} + \overline{\overline{G}}_{\text{S}} \cdot \overline{I}_l^{\text{d}} - \overline{E}_l^{\text{sca}} \right\|^2,$$

where $\overline{I}_l^{\text{d}}$ and $\overline{I}_l^{\text{a}}$ are as in (28) and (30), respectively, and $\|\cdot\|$ denotes the L^2 norm of a tensor. The current equation in (25) is another key equation to satisfy. Using the current construction (30), we define an operator as

$$(32) \qquad \left(\mathcal{L}_{\text{SOM}}^{\text{2D}}(\overline{\beta}_l) \right)_{m,n} = \frac{\overline{\overline{I}}_{l;m,n}^{\text{a}}}{-i\omega\epsilon_0} - \overline{\overline{\chi}}_{m,n} \overline{\overline{A}}_{m,n} \left(\overline{\overline{I}}_l^{\text{a}} \right),$$

where $\overline{\overline{I}}_l^{\text{a}} = \text{ten}\left\{ \overline{I}_l^{\text{a}}(\overline{\beta}_l) \right\}$, $\text{ten}\{\cdot\}$ is the inverse operation of $\text{vec}\{\cdot\}$, i.e., $\overline{\overline{I}}_{l;m,n}^{\text{a}} = \overline{I}_{l;q}^{\text{a}}$ with $q = m + (n-1) \times M_1$, $m = 1, 2, \ldots, M_1$ and $n = 1, 2, \ldots, M_2$. With this definition, we could write the mismatch of (25) as

$$(33) \qquad \Delta_l^{\text{cur}}(\overline{\beta}_l, \overline{\overline{\chi}}) = \left\| \mathcal{L}_{\text{SOM}}^{\text{2D}}(\overline{\beta}_l) - \overline{\overline{\Gamma}}_l^{\text{2D}} \right\|^2,$$

where $\overline{\overline{\Gamma}}_{l;m,n}^{\text{2D}} = \overline{\overline{\chi}}_{m,n} \left[\overline{\overline{E}}_{l;m,n}^{\text{inc}} + \overline{\overline{A}}_{m,n} \left(\overline{\overline{I}}_l^{\text{d}} \right) \right] + \frac{1}{i\omega\epsilon_0} \overline{\overline{I}}_{l;m,n}^{\text{d}}$. Finally, the objective of the optimization is to minimize the objective function

$$(34) \qquad f(\overline{\beta}_1, \overline{\beta}_2, \ldots, \overline{\beta}_{N_{\text{i}}}, \overline{\overline{\chi}}) = \sum_{l=1}^{N_{\text{i}}} \left(\Delta_l^{\text{fie}} / \left\| \overline{E}_l^{\text{sca}} \right\|^2 + \Delta_l^{\text{cur}} / \left\| \overline{\overline{E}}_l^{\text{inc}} \right\|^2 \right).$$

In [13, 44, 34], the conjugate gradient (CG) type algorithm that is used in contrast source inversion (CSI) method [39, 40] is adopted to minimize this nonlinear equation by alternatively updating the $\overline{\beta}_l$ and $\overline{\overline{\chi}}$ in every iteration of the optimization. Note that, the most computational demanding operation in every iteration is the calculation of the output of the operator A with an $M_1 \times M_2$ dimensional tensor as the input (see (26)). Due to its intrinsic convolution characteristic, it can be calculated by using the fast Fourier transform (FFT) with much less computational cost, $O(M \log_2 M)$, compared to the direct operation, $O(M^2)$, where $M = M_1 \times M_2$.

The parameter L controls the convergence rate, and there is a successive range for the value of L in which the SOM could converge at the optimal speed. This is mainly due to the fact that, when the deterministic part of the current is already obtained from the scattered fields, the dominant part of the scattered fields is automatically matched whereas the mismatch of the remaining subordinate part of the scattered fields only contribute little to the total objective function (34). The larger the L is, the smaller the mismatch of the scattering data. In this case, the algorithm only needs to construct the ambiguous part of the current within the subordinate current subspace $\overline{\overline{V}}_{\text{S}}^-$ to balance the total induced current at the first few iterations of the optimization when the mismatch of the induced current is still much larger than the mismatch of

the scattering data. Consequently, at the very beginning of the optimization, this mechanism lets the algorithm avoid simultaneously matching the scattering data and the induced current, and thus reduces the difficulty of the problem. Such a mechanism actually accelerates the optimization. Again, here we need to accentuate that if we increase the value of L so that σ_L^{S} is below the noise level, although the mismatch of the scattering data is further depressed, the noise contaminated deterministic part of the current could spoil the optimization [41].

In [23, 8, 36], the radiating and non-radiating current concept is used to address the inverse source problem, in which the radiating current is obtained either as the minimum norm solution or by the truncated SVD method. Compared to this well-known concept, the concept of the deterministic part and the ambiguous part of the induced current used in the SOM is more convenient for the numerical inversion method in the presence of noise, since, as discussed above, the parameter L can be chosen so that the deterministic part of induced current is obtained without too much being contaminated by the noise. The inclusion of the scattering data mismatch in the objective function in SOM guarantees that the current obtained by the optimization is more rectified by the physical conditions, and in the meanwhile, the effect from the noise is minimized. The key difference between the two sets of concepts is that the ambiguous part of the induced current could include both the radiating and non-radiating current.

3.2. 3D SOM. For the method of moments for 3D case, we adopt the scheme proposed in [1]. Since in this subsection we only consider non-magnetic scatterers, we only consider the simpler EFIE rather than the integral equation set in [1].

In 3D case, we similarly assume that, there are N_{i} incident waves from different angles onto the cuboid domain of interest $\mathcal{D}$ ($\mathcal{D} \subset \mathcal{R}^3$, the background 3D homogeneous medium with permittivity ϵ_0, permeability μ_0, and wave number k_0). For each incidence, the scattered fields are detected by N_{r} antennas located at $\boldsymbol{r}'_j$, $j = 1, 2, \ldots, N_{\mathrm{r}}$. For the lth incidence, the EFIE is as

$$(35) \quad [\epsilon_{\mathrm{r}}(\boldsymbol{r}) - 1]\, \boldsymbol{E}_l^{\mathrm{inc}}(\boldsymbol{r}) = \frac{\boldsymbol{I}_l(\boldsymbol{r})}{-i\omega\epsilon_0} - [\epsilon_{\mathrm{r}}(\boldsymbol{r}) - 1]\, i\omega\mu_0 \left(\overline{\overline{I}} + \frac{\nabla\nabla}{k_0^2} \right) \cdot \int_{\mathcal{D}} g(\boldsymbol{r}, \boldsymbol{r}')\boldsymbol{I}_l(\boldsymbol{r}')d\boldsymbol{r}'$$

where $\overline{\overline{I}}$ is the identity tensor, $g(\boldsymbol{r}, \boldsymbol{r}') = \exp(ik_0|\boldsymbol{r} - \boldsymbol{r}'|)/(4\pi|\boldsymbol{r} - \boldsymbol{r}'|)$ is the 3D Green's function for the background homogeneous medium, and $\boldsymbol{I}_l(\boldsymbol{r})$ and $\boldsymbol{E}_l^{\mathrm{inc}}(\boldsymbol{r})$ are the induced current and the incident electric field at $\boldsymbol{r}$, respectively. Similarly, the induced current is defined as

$$(36) \qquad\qquad \boldsymbol{I}_l(\boldsymbol{r}) = -i\omega\epsilon_0\, [\epsilon_{\mathrm{r}}(\boldsymbol{r}) - 1]\, \boldsymbol{E}_l(\boldsymbol{r}),$$

where $\boldsymbol{E}_l(\boldsymbol{r})$ is the electric field at $\boldsymbol{r}$. Compared to 2D case, the most distinguishable difference is the coupling effects between the different components of the vectorial field and current due to the operator $\overline{\overline{I}} + \frac{\nabla\nabla}{k_0^2}$. We follow the finite difference scheme in [1] to deal with such coupling, and thus the volume integration only concerns the multiplication of the scalar Green's function with each component of the induced current

$$(37) \qquad\qquad (\boldsymbol{A}\boldsymbol{I}_l)(\boldsymbol{r}) := i\omega\mu_0 \int_{\mathcal{D}} g(\boldsymbol{r}, \boldsymbol{r}')\boldsymbol{I}_l(\boldsymbol{r}')d\boldsymbol{r}',$$

which is a convolution type integration and can be computed by the 3D fast Fourier

transform (FFT). For the coupling term, we define

$$(38) \qquad (\boldsymbol{BI}_l)(\boldsymbol{r}) := \frac{\nabla\nabla \cdot (\boldsymbol{AI}_l)(\boldsymbol{r})}{k_0^2}.$$

With Eqs. (37) and (38), we can rewrite (35) as

$$(39) \qquad [\epsilon_{\mathrm{r}}(\boldsymbol{r}) - 1]\, \boldsymbol{E}_l^{\mathrm{inc}}(\boldsymbol{r}) = \frac{\boldsymbol{I}_l(\boldsymbol{r})}{-i\omega\epsilon_0} - [\epsilon_{\mathrm{r}}(\boldsymbol{r}) - 1]\,[(\boldsymbol{AI}_l)(\boldsymbol{r}) + (\boldsymbol{BI}_l)(\boldsymbol{r})].$$

And we now need to write (39) into a discretized form. To this end, we first discretize the cuboid domain of interest into many small cuboid subdomains, the center of which are located at $\boldsymbol{r}_{m,n,p}$, $m = 1, 2, \ldots, M_1$, $n = 1, 2, \ldots, M_2$ and $p = 1, 2, \ldots, M_3$. Here, M_1, M_2, and M_3 are the total number of subdomains along x, y, and z direction, respectively, and, in 3D case, we still let $M = M_1 \times M_2 \times M_3$ be the total number of the subdomains. With such discretization, (39) can be written as

$$(40) \qquad \hat{\chi}_{m,n,p}\hat{\hat{E}}_{l;m,n,p,\kappa}^{\mathrm{inc}} = \frac{1}{-i\omega\epsilon_0}\hat{\hat{I}}_{l;m,n,p,\kappa} - \hat{\chi}_{m,n,p}\left[\hat{\hat{A}}_{m,n,p,\kappa}(\hat{\hat{I}}_l) + \hat{\hat{B}}_{m,n,p,\kappa}(\hat{\hat{I}}_l)\right],$$

where the subscript $\kappa = 1, 2$, and 3 denotes the x, y, and z components of a vector. As in 2D case, the output of $\hat{\hat{A}}$ here can be obtained by 3D FFT algorithm. For further details of the discretization of (39) and the finite difference scheme to generate $\hat{\hat{B}}$ from $\hat{\hat{A}}$, please refer to the Appendix of [1].

Due to the polarization characteristics, for the lth incidence, the scattered fields in 3D scenario can be obtained by

$$(41) \qquad \overline{E}_l^{\mathrm{sca}} = \overline{\overline{G}}_{\mathrm{S}}^{\mathrm{3D}} \cdot \overline{I}_l,$$

where $\overline{E}_l^{\mathrm{sca}} = \left[\overline{E}_{l;1}^{\mathrm{scaT}}, \overline{E}_{l;2}^{\mathrm{scaT}}, \overline{E}_{l;3}^{\mathrm{scaT}}\right]^{\mathrm{T}}$ is a $3N_{\mathrm{r}}$ dimensional vector with $\overline{E}_{l;\kappa}^{\mathrm{sca}} = \left[E_{l;\kappa;1}^{\mathrm{sca}}, E_{l;\kappa;2}^{\mathrm{sca}}, \ldots, E_{l;\kappa;N_{\mathrm{r}}}^{\mathrm{sca}}\right]^{\mathrm{T}}$ ($\kappa = 1, 2, 3$ denotes the x, y, z component of the corresponding vector, respectively), $\overline{I}_l$ is a $3M$ dimensional vector obtained by $\overline{I}_l = \mathrm{vec}\left\{\hat{\hat{I}}_l\right\}$. In 3D scenario, the vectorization operation $\mathrm{vec}\{\cdot\}$ is defined to vectorize a four-dimensional tensor into a vector, i.e., if $\overline{I}_l = \mathrm{vec}\left\{\hat{\hat{I}}_l\right\}$, we have $\overline{I}_{l;\vartheta} = \hat{\hat{I}}_{l;m,n,p,\kappa}$ with $\vartheta = (\kappa - 1) \times M + (p - 1) \times (M_1 \times M_2) + (n - 1) \times M_1 + m$. In (41), the scattering operator is defined as

$$(42) \qquad \overline{\overline{G}}_{\mathrm{S}}^{\mathrm{3D}} = \left[\begin{array}{ccc} \overline{\overline{G}}_{\mathrm{S};11} & \overline{\overline{G}}_{\mathrm{S};12} & \overline{\overline{G}}_{\mathrm{S};13} \\ \overline{\overline{G}}_{\mathrm{S};21} & \overline{\overline{G}}_{\mathrm{S};22} & \overline{\overline{G}}_{\mathrm{S};23} \\ \overline{\overline{G}}_{\mathrm{S};31} & \overline{\overline{G}}_{\mathrm{S};32} & \overline{\overline{G}}_{\mathrm{S};33} \end{array}\right],$$

a $3N_{\mathrm{r}} \times 3M$ matrix, with $\overline{\overline{G}}_{\mathrm{S};uv}$, a $N_{\mathrm{r}} \times M$ matrix, the mapping from the v component of the induced current to the u component of scattered fields (the subscripts $u, v = 1, 2, 3$ are not indexed for tensor elements). The explicit expression of $\overline{\overline{G}}_{\mathrm{S};uv}$ is as

$$(43) \qquad \begin{aligned} \overline{\overline{G}}_{\mathrm{S};uv}(a, b) = {} & \frac{i\omega\mu_0}{k_0^2}\left\{\left(k_0^2 + \frac{ik_0}{R_{a,b}} - \frac{1}{R_{a,b}^2}\right)\delta(u - v) + \right. \\ & [(\boldsymbol{r}_a')_u - (\boldsymbol{r}_{m,n,p})_u][(\boldsymbol{r}_a')_v - (\boldsymbol{r}_{m,n,p})_v] \times \\ & \left.\left(-\frac{k_0^2}{R_{a,b}^2} - \frac{3ik_0}{R_{a,b}^3} + \frac{3}{R_{a,b}^4}\right)\right\} g(\boldsymbol{r}_a', \boldsymbol{r}_{m,n,p}) \end{aligned}$$

where $\delta(y)$ is 1 when $y = 0$ and is 0 otherwise, $k_0 = \omega\sqrt{\epsilon_0\mu_0}$ is wave number of the background medium, $R_{a,b} = |\boldsymbol{r}'_a - \boldsymbol{r}_{m,n,p}|$ in which $b = (p-1)\times(M_1\times M_2)+(n-1)\times M_1 + m$ with $a = 1, 2, \ldots, N_{\mathrm{r}}$, $b = 1, 2, \ldots, M$, $m = 1, 2, \ldots, M_1$, $n = 1, 2, \ldots, M_2$, and $p = 1, 2, \ldots, M_3$. Here, $(\boldsymbol{r})_u$ denotes the u component of $\boldsymbol{r}$.

As mentioned in the previous subsection, the induced current in (41) could be split into two parts, the deterministic part $\overline{I}^{\mathrm{d}}_l$ and the ambiguous part $\overline{I}^{\mathrm{a}}_l$. After operating the thin SVD on $\overline{\overline{G}}^{\mathrm{3D}}_{\mathrm{S}}$, we still have the same expression for $\overline{I}^{\mathrm{d}}$ and $\overline{I}^{\mathrm{a}}$ as (28) and (30), respectively. The only difference is that the $\overline{\overline{V}}^+$ is obtained from the thin SVD of $\overline{\overline{G}}^{\mathrm{3D}}_{\mathrm{S}}$, and the dimension of $\overline{\beta}$ now becomes $3M$. Note that, the complexity of thin SVD of $\overline{\overline{G}}^{\mathrm{3D}}_{\mathrm{S}}$ is $O(27N_{\mathrm{r}}^2 M)$. Thus, the mismatch of the scattering data in 3D case has the same expression as (31).

For the mismatch of the current equation, we need to first define an operator as

$$(44) \qquad \left(\mathcal{L}^{3D}_{\mathrm{SOM}}\left(\overline{\beta}\right)\right)_{m,n,p,\kappa} = \frac{\hat{\hat{I}}^{\mathrm{a}}_{l;m,n,p,\kappa}}{-i\omega\epsilon_0} - \hat{\chi}_{m,n,p}\left[\hat{\hat{A}}_{m,n,p,\kappa}\left(\hat{\hat{I}}^{\mathrm{a}}_l\right) + \hat{\hat{B}}_{m,n,p,\kappa}\left(\hat{\hat{I}}^{\mathrm{a}}_l\right)\right],$$

where $\hat{\hat{I}}^{\mathrm{a}}_l = \mathrm{ten}\left\{\overline{I}^{\mathrm{a}}_l(\overline{\beta}_l)\right\}$ and the $\mathrm{ten}\{\cdot\}$ is the inverse operation of $\mathrm{vec}\{\cdot\}$. Using this operator, we can define the mismatch of the current equation as

$$(45) \qquad \Delta^{\mathrm{cur}}_l(\overline{\beta}_l, \hat{\chi}) = \left\|\mathcal{L}^{3D}_{\mathrm{SOM}}(\overline{\beta}_l) - \hat{\hat{\Gamma}}^{3D}_l\right\|^2,$$

where $\hat{\hat{\Gamma}}^{3D}_{l;m,n,p,\kappa} = \frac{1}{i\omega\epsilon_0}\hat{\hat{I}}^{\mathrm{d}}_{l;m,n,p,\kappa} + \hat{\chi}_{m,n,p}\left[\hat{\hat{A}}_{m,n,p,\kappa}(\hat{\hat{I}}^{\mathrm{d}}_l) + \hat{\hat{B}}_{m,n,p,\kappa}(\hat{\hat{I}}^{\mathrm{d}}_l) + \hat{\hat{E}}^{\mathrm{inc}}_{l;m,n,p,\kappa}\right]$. The objective function in 3D case shares the same form as in 2D case that is defined in (34). We also use the CG-type optimization algorithm mentioned in the previous subsection to minimize the objective function.

3.3. The twofold SOM. In this subsection we introduce the twofold SOM in 2D TM case and its variant, the FFT twofold SOM, that can be used in both 2D and 3D cases. First, we need to introduce a new way to construct the ambiguous part of the current. From the analysis in the previous subsection, we know that in the SOM the ambiguous part of the current is constructed within a current subspace spanned by the remaining $M - L$ bases obtained from $\overline{\overline{G}}_{\mathrm{S}}$. Due to the fact that all these current bases correspond to the small singular values of the mapping, as long as the value of L is large enough, the contribution from the ambiguous part of the current to the scattered fields is small. However, this part of the induced current may still be influential to the fields inside the domain of interest, as seen from (23). In other words, the existence of the ambiguous part of the current balances the total induced current inside the domain of interest by making it satisfy the Lippmann-Schwinger equation. Besides, from (25), it is also clearly that the influence from the induced current to the fields inside the domain of interest is via the integral operator $\overline{\overline{A}}$. Bearing these, it is possible to construct $\overline{I}^{\mathrm{a}}_l$ only within a subspace that is influential to the fields inside the domain of interest, whose dimension may be much smaller than the one used in (29). To achieve this, we need to analyze the spectral property of the $\overline{\overline{A}}$ mapping, or its matrix form $\overline{\overline{G}}_{\mathrm{D}}$. The singular value decomposition (SVD) of $\overline{\overline{G}}_{\mathrm{D}}$ reads $\overline{\overline{G}}_{\mathrm{D}} \cdot \overline{v}^{\mathrm{D}}_j = \sigma^{\mathrm{D}}_j \overline{u}^{\mathrm{D}}_j$, $j = 1, 2, \ldots, M$, with $\overline{v}^{\mathrm{D}}_j$ spanning the current space and $\overline{u}^{\mathrm{D}}_j$ the field space. Here the superscript D denotes the mapping $\overline{\overline{G}}_{\mathrm{D}}$. With the

assumption that the singular values are a descending sequence, the first few, say M_0, current bases, $\overline{v}_j^{\mathrm{D}}$, $j \leq M_0$, is influential to the fields inside the domain of interest, and we can use these bases to construct the ambiguous current. On the other hand, since we already used (27) and (28) to obtain the deterministic part of the induced current, the bases used to construct the ambiguous part of the current should not include those components in the deterministic part. Thus, we can express the ambiguous part of the induced current in this way:

$$(46) \qquad \overline{I}_l^{\mathrm{a}} = \sum_{j=1}^{M_0} \overline{v}_j^{\mathrm{D}\prime} \gamma_{j,l} = \overline{\overline{V}}_{\mathrm{D}}^{+\prime} \cdot \overline{\gamma}_l,$$

where we have defined

$$(47) \qquad \begin{aligned} \overline{\overline{V}}_{\mathrm{D}}^{+\prime} &= [\overline{v}_1^{\mathrm{D}\prime}, \overline{v}_2^{\mathrm{D}\prime}, \ldots, \overline{v}_{M_0}^{\mathrm{D}\prime}] \\ &= \overline{\overline{V}}_{\mathrm{S}}^{-} \cdot \overline{\overline{V}}_{\mathrm{S}}^{-*} \cdot [\overline{v}_1^{\mathrm{D}}, \overline{v}_2^{\mathrm{D}}, \ldots, \overline{v}_{M_0}^{\mathrm{D}}] \\ &= \overline{\overline{V}}_{\mathrm{S}}^{-} \cdot \overline{\overline{V}}_{\mathrm{S}}^{-*} \cdot \overline{\overline{V}}_{\mathrm{D}}^{+} \\ &= \left(\overline{\overline{I}}_M - \overline{\overline{V}}_{\mathrm{S}}^{+} \cdot \overline{\overline{V}}_{\mathrm{S}}^{+*} \right) \cdot \overline{\overline{V}}_{\mathrm{D}}^{+}, \end{aligned}$$

and $\overline{\overline{I}}_M$ is the M dimensional identity matrix. Here, we still use superscript $+$ to denote the dominant current subspace for the mapping $\overline{\overline{G}}_{\mathrm{D}}$, and the $\overline{\gamma}_l$ is an M_0 dimensional vector. Thus, by using such construction of the ambiguous part of the induced current, the optimization is searching the current within an M_0 dimensional subspace.

Such SOM with second fold subspace constraint on the induced current is referred to as the twofold SOM (TSOM). It is found that [45], the second-fold subspace constraint on the ambiguous part of the induced current works as regularization which is able to further stabilize the optimization and increase the robustness of the inversion against noise.

However, in the TSOM, in order to obtain the bases that span the current subspace, we need to perform a singular value decomposition (SVD) of the operator that maps the induced current to the electric fields inside the domain of interest. Since the computational cost of such SVD operation is very high, $O(M^3)$, where M is the number of subdomains, it is almost prohibitive to efficiently apply the TSOM to solve the inverse scattering problems with large amount of unknowns, such as the three-dimensional electromagnetic inverse problems.

To overcome this drawback, we need to find another way to construct the current subspace instead of using the SVD operation. Notice that, as aforementioned, the purpose of using the second-fold subspace constraint is to further regularize or stabilize the optimization by rejecting those current components in the subordinate current subspace spanned by singular vectors with small singular values, say $\overline{\overline{V}}_{\mathrm{D}}^{-}$. Thus, we may approximate the original current subspace spanned by the singular vector basis by a new current subspace so that the new one still works as the original one, i.e., to exclude most of the current components in the subordinate current subspace $\overline{\overline{V}}_{\mathrm{D}}^{-}$. In [46], it is found that the current subspace spanned by the discrete Fourier bases is a very good approximation. After implementing such new current subspace in the TSOM, we significantly reduce the computational cost from the following two aspects:

1. Since we use discrete Fourier bases to construct the current subspace, we avoid the SVD operation of the matrix operator that maps the induced current to the electric field inside the domain of interest.

2. Since the discrete Fourier bases are used as the new current bases, the procedure to construct the ambiguous part of the induced current is the inverse discrete Fourier transform that can be accomplished by using the fast Fourier transform (FFT) algorithm.

The new algorithm is referred to as the FFT-TSOM, and it can solve, in an efficient manner, the 2D and 3D electromagnetic inverse scattering problems. The FFT-TSOM inherits the merits of the TSOM, better stability during the inversion and better robustness against noise compared to the SOM, and in the meanwhile has much lower computational complexity than the original TSOM. Details can be found in [46].

4. Numerical simulations.

4.1. Point-like scatterers. The following simulation shows the advantage of the proposed MUSIC method over the standard MUSIC, where the former produces higher imaging resolution than the latter does. Numerical simulations in two scenarios, noise free case and noise-contaminated case, are investigated.

We assume that three small spheres are located at $\overline{r}_1 = (0.084\lambda, 0.196\lambda, 0.084\lambda)$, $\overline{r}_2 = (-0.168\lambda, -0.056\lambda, -0.112\lambda)$ and $\overline{r}_3 = (-0.196\lambda, -0.084\lambda, 0.140\lambda)$, the first two of which are isotropic spheres with permittivity $\epsilon_1 = \epsilon_2 = 2\epsilon_0$, while the third is a rotated anisotropic sphere with permittivity tensor $\overline{\overline{\epsilon}}_3 = \texttt{diag}[\epsilon_0, 3\epsilon_0, 9\epsilon_0]$ and rotation Euler angles [43] $(\psi, \phi, \theta) = (\pi/4, \pi/3, 3\pi/8)$. These three spheres are electrically small with the same radius $a = \lambda/30$. Note that the smallest distance between the centers of spheres is 0.255λ (the distance between the second and the third one), and, for the convenience in depicting the test results, all three spheres are chosen to locate in the $y = x + 0.112\lambda$ plane. It is easily seen from the constitutive parameters of the scatterers that there are up to eight independent secondary sources induced inside the three scatterers.

There are 16 antenna units employed in this simulation, half of which are aligned along the y axis while the other half aligned along the z axis in the $x = -13\lambda$ plane. The two linear arrays are centered at $(-13\lambda, -9\lambda, 11\lambda)$ with 5λ separation distance between neighboring units.

For the noise free case, the singular values of the MSR matrix are shown in Fig.1(a), in which we see that the first eight singular values are much larger than the rest, since they are corresponding to the eight singular vectors spanning the signal space. Fig.1(b), Fig.1(c) and Fig.1(d) are the pseudo-spectrum in $y = x + 0.112\lambda$ plane obtained by the standard MUSIC method using x-, y- and z-oriented test dipole, respectively. Not surprisingly, the standard MUSIC algorithm can only find the first two isotropic spheres and fail to locate the third degenerate anisotropic target. Here, we plot the base 10 logarithm of it, and the horizontal and vertical axes in Fig.1(b), Fig.1(c) and Fig.1(d) are the x and z coordinate of spatial points in $y = x + 0.112\lambda$ plane, so do the cases hereafter. In comparison, the pseudo-spectrum obtained by the proposed MUSIC algorithm are shown in Fig.2 with $L = 4$, 5, 6 and 7. From these results, we see that, to locate the first two isotropic spheres, we only need $L = 6$, but, to locate the third degenerate anisotropic sphere, we need $L = 7$. This is due to the reason that when locating one of the first two isotropic spheres, the rest two spheres have only five independent induced dipoles, which means that $L = 6$ is sufficient for the governing equation (15) to have exact solutions; but, if we want to locate the third degenerate sphere, the rest two isotropic spheres have totally six independent
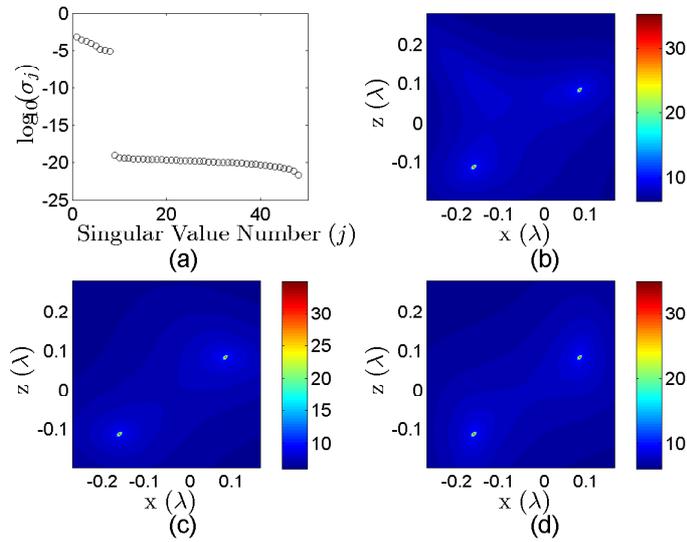
Fig. 1: Singular values and pseudo-spectrum obtained by the standard MUSIC algorithm in noise free case. (a) The 10 base logarithm of the singular values of the MSR matrix ($j = 1, 2, \ldots, 48$). (b), (c) and (d) are the 10 base logarithm of the pseudo-spectrum in $y = x + 0.112\lambda$ plane obtained by the standard MUSIC algorithm with test dipoles in x, y and z directions, respectively.
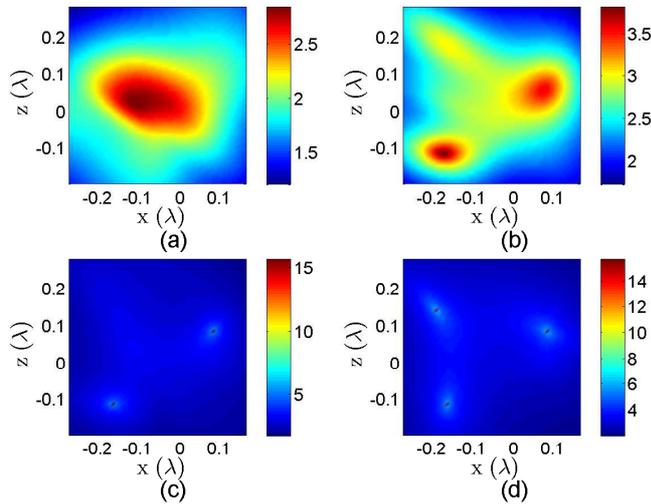
Fig. 2: Pseudo-spectrum obtained by the proposed MUSIC algorithm in noise free case. (a), (b), (c) and (d) are the 10 base logarithm of the pseudo-spectrum in $y = x + 0.112\lambda$ plane obtained by the proposed MUSIC algorithm corresponding to the $L = 4, 5, 6$ and 7 cases, respectively.
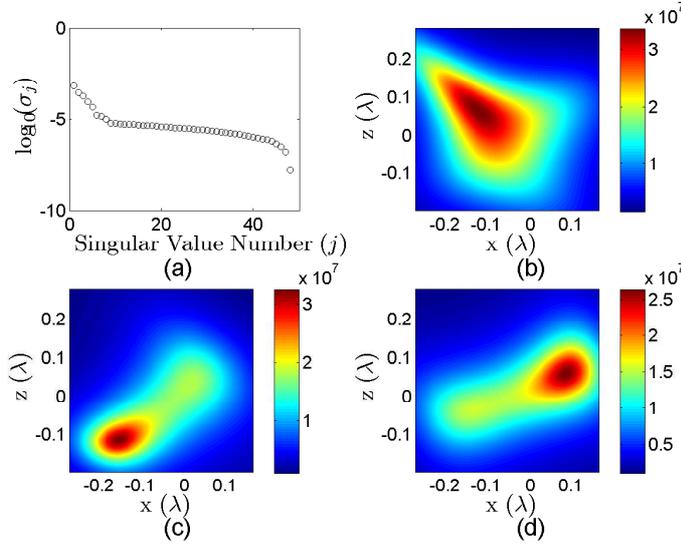
Fig. 3: Singular values and pseudo-spectrum obtained by the standard MUSIC algorithm in noise-contaminated case (30dB). (a) The 10 base logarithm of the singular values of the MSR matrix ($j = 1, 2, \ldots, 48$). (b), (c) and (d) are the pseudo-spectrum in $y = x + 0.112\lambda$ plane obtained by the standard MUSIC algorithm with test dipoles in x, y and z directions, respectively.

induced dipoles, thus only when $L = 7$ can we solve (15). For the $L = 4$ and 5 cases, since the L is not large enough to solve the governing equation, none of the three scatterers can be located precisely. If L is further increased to 8 and 9, the result will be almost the same as the one in $L = 7$ case, which are not presented here.

For the noise-contaminated case, we add additive white Gaussian noise to the MSR matrix [43]. In this simulation, 30dB white Gaussian noise is added. Fig.3(a) shows the singular values of the noise-contaminated MSR matrix, in which the singular values corresponding to the noise space are much larger than those in the noise free case. In such a case, if we apply the standard MUSIC algorithm to locate the scatterers, the pseudo-spectrum obtained by the test dipoles in x, y and z direction are shown in Fig.3(b), Fig.3(c) and Fig.3(d), respectively, which show that all the three test dipole directions fail to locate any of the three scatterers. By using the proposed MUSIC algorithm, the pseudo-spectrum are drawn in Fig.4. In Fig.4, for the $L = 4$, 5, 6 and 7 cases, image patterns are similar to those in noise-free case shown in Fig.2. However, for the $L = 8$ and 9 cases, some unwanted disturbance appear in between the second and the third spheres, which shows that the singular vector corresponding to the eighth singular value is contaminated by the noise to an extent so that it cannot be regarded as in the signal space anymore.

After locating positions, we will estimate the scattering strengths of point-like scatterers. The numerical simulations in Section 4 of [43] and Section 4 of [10] have shown the accuracy of the proposed two-step least squares method, where the scattering strengths of scatterers are reconstructed with low computational cost.
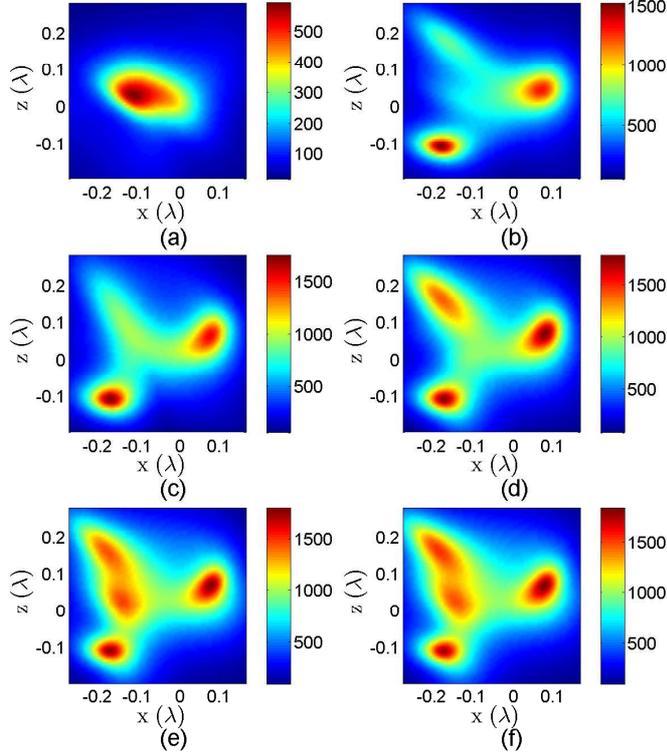
Fig. 4: Pseudo-spectrum obtained by the proposed MUSIC algorithm in noise-contaminated case (30dB). (a), (b), (c), (d), (e) and (f) are the pseudo-spectrum in $y = x + 0.112\lambda$ plane obtained by the proposed MUSIC algorithm corresponding to the $L = 4, 5, 6, 7, 8$ and 9 cases, respectively.

4.2. Extended scatterers. We present two numerical simulations for the SOM, in 2D TM and 3D scenarios. The numerical models for the forward problem in following simulations are the coupled dipole method (CDM). As mentioned at the beginning of the previous section, this does not affect the essence of the SOM.

In the 2D TM case, the 'Austria' profile, as illustrated in Fig. 5 is considered. The obstacles under study are contained in a square test domain of 2×2 m^2. The 'Austria' profile consists of two discs and one ring. The discs of radius 0.2 m are centered at $(0.3, 0.6)$ m and $(-0.3, 0.6)$ m. The ring has an exterior radius of 0.6 m and an inner radius of 0.3 m, and is centered at $(0, -0.2)$ m. The background is air and the contrast between the obstacles and the background has a value of 1 (or $\epsilon_r = 2$). 16 line sources and 32 line receivers are equally placed on a circle of radius 3 m centered at $(0, 0)$ m. In the forward scattering problem, the data are generated numerically using the CDM method with a 100×100 grid mesh, which is much finer than the one used in the inverse process (64×64) in order to avoid the inverse crime [19]. The scattering data generated in the forward process are recorded in the format of the multistatic response (MSR) matrix $\overline{\overline{K}}$ whose size is $N_s \times N_i$. Then additive white Gaussian noise is added to the MSR matrix, and the resultant noisy matrix is treated as the measured MSR matrix and is used to reconstruct scatterers [43]. The operating frequency is 400
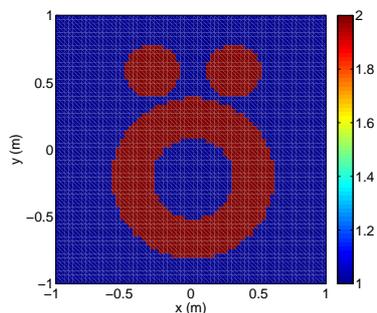
Fig. 5: Inverse experiment of the Austria profile: exact profile.
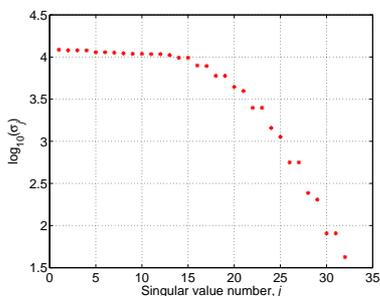
Fig. 6: The spectrum of the operator $\overline{\overline{G}}_{\mathrm{S}}$, where the base 10 logarithm of the singular value is plotted.
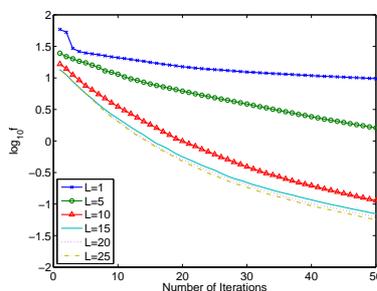
Fig. 7: The comparison of convergence trajectories in the first 50 iterations for different value of L, where the base 10 logarithm of the objective function value is plotted.

MHz, and the proposed method works directly on the data without using frequency-hopping. A priori information is that the scatterers are lossless and have non-negative contrasts [39]. One of the key components of the SOM is the spectrum analysis. In particular, the value of L is determined from the spectrum. The spectrum of $\overline{\overline{G}}_{\mathrm{S}}$ corresponding to the aforementioned simulation configuration is shown in Fig. 6. First, in the absence of noise, the convergence is compared for different value of L in the first 50 iterations and the results are shown in Fig. 7. It is observed that the increase of the value of L results in a faster convergence. The reconstructed relative permittivity profiles are shown in Fig. 8. The cases of $L = 10, 15, 20$ and 25 produce successful reconstruction results. Numerical simulations show that the cases of $L = 1$ and 5 also produce successful reconstruction results, however at the expense of more iterations, especially for the case of $L = 1$, which in this test costs 800 iterations to achieve that. Both Fig. 7 and Fig. 8 indicate that there is no noticeable difference between the results for $L = 15, 20$, and 25.

Next, the proposed algorithm is tested for noise-contaminated data. The reconstruction results for 10%, 30%, and 50% additive white Gaussian noise are shown in Fig. 9, where L is equal to 15. The optimization iteration is terminated when there is no significant improvement in the objective function in consecutive two iterations.

(a) $L = 1$ (c) $L = 10$ (e) $L = 20$

(b) $L = 5$ (d) $L = 15$ (f) $L = 25$
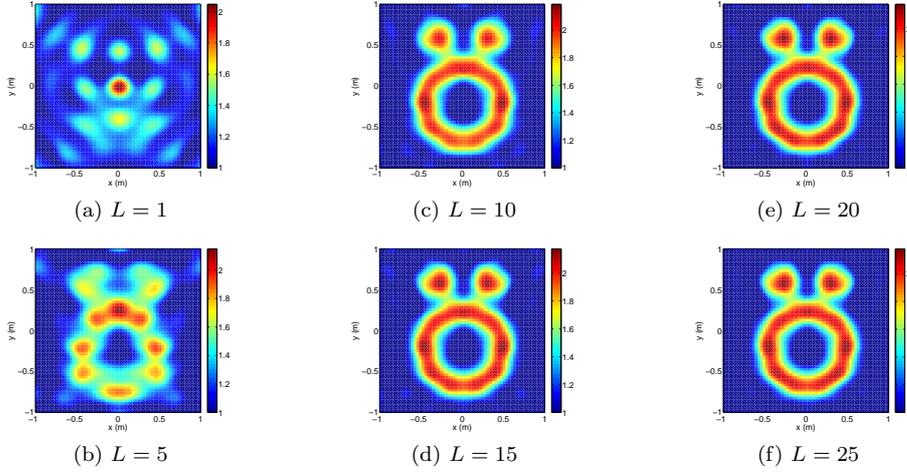
Fig. 8: Reconstructed relative permittivity profiles at the 50th iteration for different values of L.

(a) 10% noise   (b) 30% noise   (c) 50% noise
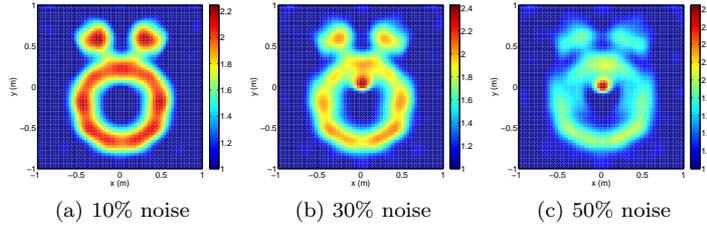
Fig. 9: Reconstructed relative permittivity profiles for $L = 15$ at different noise levels. The optimization is terminated when there is no significant improvement in the objective function in consecutive two iterations, which are 59, 31, and 21, respectively for the three noise levels.

For the three noise levels, the numbers of iterations are 59, 31, and 21, respectively. The reconstruction is successful in case of 10% noise. The result in case of 30% noise is also satisfying, except that an artifact appears in the inner upper of the annulus. In case of 50% noise, the artifact is more prominent and a portion of the upper annulus is almost disjointed from the rest. Nevertheless, the positions of the disks and the annulus are correctly determined. In particular, the hole inside the annulus and the gap between the rings and the annulus can be easily identified.

For 3D case, the scatterer used in the simulation is a coated cube centered at the origin with its inner edge length $a = 0.6\lambda$ and outer edge length $b = 1.6\lambda$ (λ is the wavelength of the incident wave in the background medium, air), as shown in Fig. 10. The relative permittivity of the inner layer is $\epsilon_{r1} = 1.6$ while the relative permittivity of the outer layer is $\epsilon_{r2} = 1.3$. Note that though we use non-conductive scatterer, we do not assume so during our inversion procedure. The coated cube is illuminated by 30 electric dipole antennas, which are located on three circles (with 10 dipoles evenly
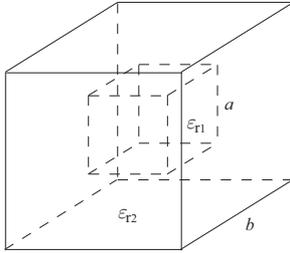
Fig. 10: A coated cube.
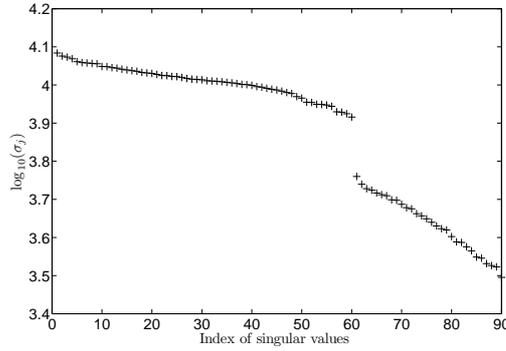
Fig. 11: Singular values of $\overline{\overline{G}}_{\mathrm{S}}^{\mathrm{3D}}$.

distributed on each circle) with the same radius 3λ. The three circles are in $x - y$, $y - z$ and $z - x$ planes, and their centers are at $(0.2\lambda, 0, -0.1\lambda)$, $(0.1\lambda, 0, -0.15\lambda)$ and $(-0.05\lambda, 0.1\lambda, 0)$, respectively. The direction of the electric dipole sources in $x - y$ plane are in z direction, while those in $y - z$ and $z - x$ planes are in x and z direction, respectively. Scattered fields are detected by 30 detectors, which are located at the same positions as the 30 dipole sources. As mentioned at the beginning of the previous section, we assume that each detector measures the vectorial electric field in three directions. Thus, we have 30×90 data points. These synthetic data are calculated by the MOM-based algorithm proposed in [1] using $60 \times 60 \times 60$ mesh grid of a cubic domain containing the scatterer. This cubic domain is centered at the origin and with an edge length 3λ. In this simulation, 10% additive white Gaussian noise is added.

We choose the same cubic domain as the domain of interest during our inversion procedure. The domain of interest is discretized into a $30 \times 30 \times 30$ mesh grid, which means we have 27000 unknowns in total. After concreting the locations of detectors
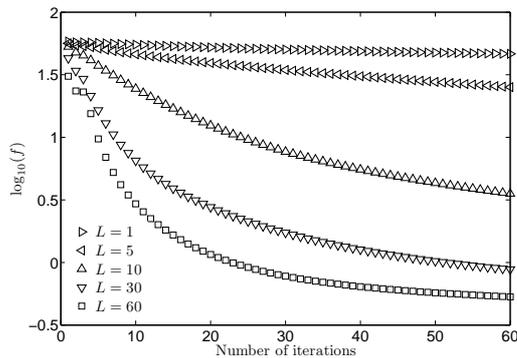
Fig. 12: The objective function values within 60 iterations when $L = 1, 5, 10, 30$ and 60.

and all the subdomains, we can generate $\overline{\overline{G}}_{\mathrm{S}}^{3D}$ and its singular values, as shown in
Fig. 11. From Fig. 11, we see that there is a gap between the first 60 singular values
and the last 30 singular values. This is due to the fact that all the detectors are
located in the far-field zone of the domain of interest, thus the radial components
of scattered fields are weaker than the tangential components, the former of which
span the subspace corresponding to those subordinate singular values. In addition,
we have numerically verified that, the gap increases when we increase the radius of
the three circles where the detectors are located. In this simulation, we test five
different values of L, i.e., $L = 1, 5, 10, 30$ and 60, and for all these cases the initial
guesses are the background medium, air. The values of the objective function within
60 iterations are shown in Fig. 12, from which we clearly see that, the larger the
value of L, the faster the objective function converges. The retrieval results for these
different cases after 60 iterations are shown in Fig. 13 and 14. In Fig. 13, the real
part of the retrieval dielectric profile is presented. Sub-figures from the first row to the
fifth row are corresponding to the cases of $L = 1, 5, 10, 30$ and 60, respectively. The
sub-figures in the first, second and third column are the cross section at $z = -0.05\lambda$,
$y = -0.05\lambda$, and $x = -0.05\lambda$, respectively. We apply the same rule to the sub-figures
in Fig. 14 in which the imaginary part of the retrieval dielectric profile is presented.
From these two figures, we clearly see that, when $L = 60$, we obtain a satisfactory
retrieval result. From this simulation, we can conclude that, in 3D scenario, the SOM
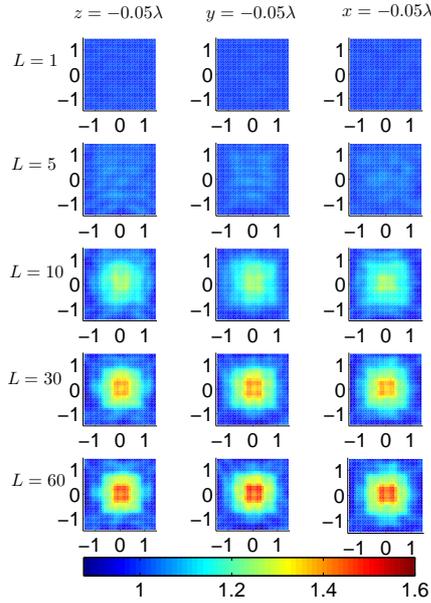
Fig. 13: The real part of the retrieval result of the dielectric profile for the domain of interest after 60 iterations. The real part of the relative permittivity of the inner cube and outer layer are 1.6 and 1.3, respectively.
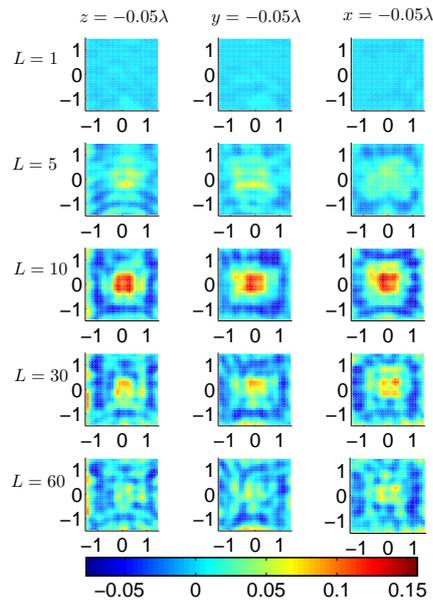
Fig. 14: The imaginary part of the retrieval result of the dielectric profile for the domain of interest after 60 iterations. The imaginary part of the relative permittivity of the inner cube and outer layer are both 0.

behaves the same as it does in 2D TM case, and the SOM can efficiently solve the 3D electromagnetic inverse scattering problems in a small number iterations.

For numerical tests of the TSOM in 2D TM case, readers are referred to the reference [45], and for FFT-TSOM in both 2D and 3D cases, readers are referred to [46], in which the better stability and good robustness against noise of the two algorithms are presented.

5. Conclusion and discussion. The inverse scattering problem of reconstructing point-like scatterers is distinctly different from that of reconstructing extended scatterers. The key difference is the current-to-field mapping operator. The operator is injective for point-like scatterers, whereas it is compact for extended scatterers. Due to this key difference, point-like scatterers can be reconstructed noniteratively. The MUSIC is applied to locate scatterers, where the Green's function vectors evaluated at scatterers span a subspace that coincides with the range (subspace) of the MSR matrix. A two-step least squares method is applied to retrieve the scattering strengths of point-like scatterers. Since there is no forward problem iteratively evaluated in both the MUSIC and the two-step least squares method, the inverse problem is solved with low computational cost. In comparison, the inverse problem of reconstructing extended scatterers has to be cast into an optimization problem and be solved iteratively. Although the induced current cannot be uniquely determined from the scattered field, a portion of it can be uniquely determined. This portion corresponds to the subspace spanned by the singular vectors of the current-to-field mapping operator associated with few leading singular values. The complementary orthogonal subspace is obtained by optimization method. Due to aforementioned reasons, the SOM is fast convergent, robust in presence of noise, being high resolution, and able to reconstruct scatterers of complex patterns. Numerical simulations validate the algorithms. Based on the SOM, the TSOM and the FFT-TSOM are introduced in order to achieve better stability and better robustness against noise for the inversion.

The MUSIC and two-step least squares method can also be generalized to solve phaseless (intensity only) inverse scattering problems [31, 11]. In addition, they can be applied to inverse scattering problems with inhomogeneous backgrounds as well [16]. The SOM has been further extended to deal with inverse scattering problems in 2D transverse electric (TE) scenario for both isotropic scatterers [32], and anisotropic scatterers [3], as well as the electric impedance tomography problem [14]. Besides, the SOM has been applied to reconstruct perfect conducting scatterers by using a properly defined objective function [42]. The SOM has also been used to solve the inverse scattering problems with inhomogeneous background [17], the through-wall imaging problem [29], and the inverse scattering problem with phaseless data [33]. Here, it is worth mentioning that, when solving the inverse scattering problems with phaseless data, we use an optimization method to obtain the deterministic part of the induced current, since the measured data is no longer a linear function of the induce current. Details can be found in [33]. Recent paper [25] shows that the MUSIC algorithm is amenable to extended scatterers as well. Our experiences in this regard are that there are conditions for MUSIC to be able to reconstruct extended scatterers, such as it requires sufficiently large apertures of incidence and measurement, scatterers cannot be annulus-like, and two scatterers cannot be too close to each other. Finally, it is interesting to investigate the inverse scattering problem where both point-like and extended scatterers are present. To the best of authors' knowledge, there has been no such technical literature reported so far. If the scattering strength of point-like scatterer is not strong enough, we can hardly identify it due to presence of noise. Thus,

we consider only point-like scatterers with strong scattering strengthes. To solve such a mixed scatterer problem, we may consider two approaches: (1) First apply MUSIC to identify the positions of point-like scatterers and then apply optimization algorithms to reconstruct both scattering strength of point-like scatterers and permittivities of extended scatterers; (2) Treat each point-like scatterer as one cell of discretized domain and apply optimization methods to reconstruct the permittivity of each cell. Mixed scatterer is one of our future research topics in inverse scattering.

REFERENCES

[1] A. Abubakar and P. M. van den Berg, *Iterative forward and inverse algorithms based on domain integral equations for three-dimensional electric and magnetic objects,* J. Comp. Phys., 195 (2004), pp. 236–262.

[2] K. Agarwal and X. Chen, *Applicability of MUSIC-type imaging in two-dimensional electromagnetic inverse problems,* IEEE Trans. Antennas Propag., 56 (2008), pp. 3217–3223.

[3] K. Agarwal, L. Pan, and X. Chen, *Subspace-based optimization method for reconstruction of two-dimensional complex anisotropic dielectric objects*, IEEE Trans. Microwave Theory and Technique, 58 (2010), pp. 1065–1074.

[4] H. Ammari and H. Kang, *Reconstruction of Small Inhomogeneities from Boundary Measurements*, Berlin: Springer-Verlag, 2004.

[5] H. Ammari, E. Iakovleva, and H. Kang, *Reconstruction of a small inclusion in a two-dimensional open waveguide*, SIAM J. Appl. Math., 65 (2005), pp. 2107–2127.

[6] H. Ammari, E. Iakovleva, and D. Lesselier, *A MUSIC algorithm for locating small inclusions buried in a half-space from the scattering amplitude at a fixed frequency*, SIAM Mult. Model. and Simu., 3 (2005), pp. 597–628.

[7] H. Ammari, E. Iakovleva, D. Lesselier, and G. Perruson, *MUSIC-type electromagnetic imaging of a collection of small three-dimensional bounded inclusions*, SIAM J. Sci. Comput., 29:2 (2007), pp. 674–709.

[8] S. Caorsi and G. Gragnani, *Inverse-scattering method for dielectric objects based on the reconstruction of the nonmeasurable equivalent current density*, Radio Sci., 34 (1999), pp. 1–8.

[9] X. Chen and Y. Zhong, *A robust noniterative method for obtaining scattering strengths of multiply scattering point targets*, J. Acoust. Soc. Am., 122 (2007), pp. 1325–1327.

[10] X. Chen and Y. Zhong, *Electromagnetic imaging of multiple-scattering small objects: Non-iterative analytical approach*, Journal of Physics: Conference Series, 124 (2008), p. 012016 (12 pages).

[11] X. Chen, *Signal-subspace method approach to intensity-only electromagnetic inverse scattering problem*, J. Opt. Soc. Am. A, 25 (2008), pp. 2018–2024.

[12] X. Chen, *Application of signal-subspace and optimization methods in roconstructing extended scatterers*, J. Opt. Soc. Am. A, 26 (2009), pp. 1022–1026.

[13] X. Chen, *Subspace-based optimization method for solving inverse scattering problems*, IEEE Trans. Geosci. Remote Sens., 48 (2010), pp. 42–49.

[14] X. Chen, *Subspace-based optimization method in electric impedance tomography*, J. of Electromagn. Waves and Appl., 23 (2009), pp. 1397–1406.

[15] X. Chen and Y. Zhong, *MUSIC electromagnetic imaging with enhanced resolution for small inclusions*, Inverse Probl., 25 (2009), p. 015008.

[16] X. Chen, *Multiple signal classification method for detecting point-like scatterers embedded in an inhomogeneous background medium*, J. Acoust. Soc. Am., 127 (2010), pp. 2392–2397.

[17] X. Chen, *Subspace-based optimization method for inverse scattering problems with an inhomogeneous background medium*, Inverse Probl., 26 (2010), pp. 074007.

[18] M. Cheney, *The linear sampling method and the MUSIC algorithm*, Inverse Probl., 17 (2001), pp. 591–595.

[19] D. Colton and R. Kress, *Inverse Acoustic and Electromagnetic Scattering Theory*, Berlin, Germany: Springer-Verlag, second ed., 1998.

[20] A. J. Devaney, *Super-resolution processing of multi-static data using time-reversal and MUSIC*, available at `http://www.ece.neu.edu/faculty/devaney/ajd/preprints.htm`, 2000.

[21] A. J. Devaney, *Time reversal imaging of obscured targets from multistatic data*, IEEE Trans. Antennas Propag., 53 (2005), pp. 1600–1610.

[22] A. J. Devaney, E. A. Marengo, and F. K. Gruber, *Time-reversal-based imaging and inverse scattering of multiply scattering point targets*, J. Acoust. Soc. Am., 118 (2005), pp. 3129–3138.

[23] T. Habashy, M. Oristaglio, and A. de Hoop, *Simultaneous nonlinear reconstruction of two-dimensional permittivity and conductivity*, Radio Sci., 29 (1994), pp. 1101–1118.

[24] A. Horn and C. R. Johnson, *Matrix Analysis*, Cambridge, UK: Cambridge University Press, 1985.

[25] S. Hou, K. Solna and H. Zhao, *A direct imaging algorithm for extended targets*, Inverse Probl., 22 (2006), pp. 1151–1178.

[26] E. Iakovleva, S. Gdoura, D. Lesselier, and G. Perrusson, *Multistatic response matrix of a 3-D inclusion in half space and MUSIC imaging*, IEEE Trans. Antennas Propag., 55 (2007), pp. 2598–2609.

[27] A. Kirsch, *The MUSIC-algorithm and the factorization method in inverse scattering theory for inhomogeneous media*, Inverse Probl., 18 (2002), pp. 1025–1040.

[28] J. A. Kong, *Electromagnetic Wave Theory*, Cambridge, MA: EMW, 2000.

[29] T. Lu, K. Agarwal, Y. Zhong, and X. Chen, *Through-wall imaging: application of subspace-based optimization method*, Progress in Electromagnetic Research, 102 (2010), pp. 351–366.

[30] E. A. Marengo and F. K. Gruber, *Noniterative analytical formula for inverse scattering of multiply scattering point targets*, J. Acoust. Soc. Am., 120 (2006), pp. 3782–3788.

[31] E. A. Marengo, R. D. Hernandez, and H. Lev-Ari, *Intensity-only signal-subspace-based imaging*, J. Opt. Soc. Am. A, 24 (2007), pp. 3619–3635.

[32] L. Pan, K. Agarwal, Y. Zhong, S. P. Yeo, and X. Chen, *Subspace-based optimization method for reconstructing extended scatterers: Transverse electric case*, J. Opt. Soc. Am. A, 26 (2009), pp. 1932–1937.

[33] L. Pan, Y. Zhong, X. Chen, and S. P. Yeo, *Subspace-based optimization method for inverse scattering problems utilizing phaseless data*, IEEE Trans. Geosci. Remote Sens., 49 (2011), pp. 981–987.

[34] L. Pan, X. Chen, Y. Zhong, and S. P. Yeo, *Comparison among the variants of subspace-based optimization method for addressing inverse scattering problems: transverse electric case*, J. Opt. Soc. Am. A, 27 (2010), pp. 2208–2215.

[35] A. F. Peterson, S. L. Ray, and R. Mittra, *Computational Methods for Electromagnetics*, New York, US, 1998.

[36] P. Rocca, M. Donelli, G. Gragnani, and A. Massa, *Iterative multi-resolution retrieval of non-measurable equivalent currents for the imaging of dielectric objects*, Inverse Probl., 25 (2009), 055004.

[37] R. O. Schmidt, *Multiple emitter location and signal parameter estimation*, IEEE Trans. Antennas Propag., 34 (1986), pp. 276–280.

[38] F. Simonetti, *Multiple scattering: The key to unravel the subwavelength world from the far-field pattern of a scattered wave*, Phys. Rev. E, 73 (2006), p. 036619.

[39] P. M. van den Berg and R. E. Kleinman, *A contrast source inversion method*, Inverse Probl., 13 (1997), pp. 1607–1620.

[40] P. M. van den Berg, A. L. van Broekhoven, and A. Abubakar, *Extended constrast source inversion*, Inverse Probl., 15 (1999), pp. 1325–1344.

[41] X. Ye and X. Chen, *The role of regularization parameter of subspace-based optimization method in solving inverse scattering problems*, in "Proc. Asia-Pacific Microwave Conf.", Singapore, Dec. 2009, pp. 1549–1552.

[42] X. Ye, X. Chen, Y. Zhong, and K. Agarwal, *Subspace-based optimization method for reconstructing perfectly electric conductors*, Progress in Electromagnetic Research, 100 (2010), pp. 119–128.

[43] Y. Zhong and X. Chen, *MUSIC imaging and electromagnetic inverse scattering of multiply scattering small anisotropic spheres*, IEEE Trans. Antennas Propag., 55 (2007), pp. 3542–3549.

[44] Y. Zhong, X. Chen, and K. Agarwal, *An improved subspace-based optimization method and its implementation in solving three-dimensional inverse problems*, IEEE Trans. Geosci. Remote Sens., 48 (2010), pp. 3763–3768.

[45] Y. Zhong and X. Chen, *Twofold subspace-based optimization method for solving inverse scattering problems*, Inverse Probl., 25 (2009), pp. 085003.

[46] Y. Zhong, and X. Chen, *An FFT twofold subspace-based optimization method for solving electromagnetic inverse scattering problems*, IEEE Trans. Antennas Propag., 59 (2011), pp. 914–927.